NASA/CR—2003-212311

Inflow/Outflow Conditions for Unsteady Aerodynamics and Aeroacoustics in Nonuniform Flow

Oliver V. Atassi
Pratt & Whitney, East Hartford, Connecticut

December 2003

The NASA STI Program Office . . . in Profile

Since its founding, NASA has been dedicated to the advancement of aeronautics and space science. The NASA Scientific and Technical Information (STI) Program Office plays a key part in helping NASA maintain this important role.

The NASA STI Program Office is operated by Langley Research Center, the Lead Center for NASA's scientific and technical information. The NASA STI Program Office provides access to the NASA STI Database, the largest collection of aeronautical and space science STI in the world. The Program Office is also NASA's institutional mechanism for disseminating the results of its research and development activities. These results are published by NASA in the NASA STI Report Series, which includes the following report types:

- TECHNICAL PUBLICATION. Reports of completed research or a major significant phase of research that present the results of NASA programs and include extensive data or theoretical analysis. Includes compilations of significant scientific and technical data and information deemed to be of continuing reference value. NASA's counterpart of peer-reviewed formal professional papers but has less stringent limitations on manuscript length and extent of graphic presentations.

- TECHNICAL MEMORANDUM. Scientific and technical findings that are preliminary or of specialized interest, e.g., quick release reports, working papers, and bibliographies that contain minimal annotation. Does not contain extensive analysis.

- CONTRACTOR REPORT. Scientific and technical findings by NASA-sponsored contractors and grantees.

- CONFERENCE PUBLICATION. Collected papers from scientific and technical conferences, symposia, seminars, or other meetings sponsored or cosponsored by NASA.

- SPECIAL PUBLICATION. Scientific, technical, or historical information from NASA programs, projects, and missions, often concerned with subjects having substantial public interest.

- TECHNICAL TRANSLATION. English-language translations of foreign scientific and technical material pertinent to NASA's mission.

Specialized services that complement the STI Program Office's diverse offerings include creating custom thesauri, building customized databases, organizing and publishing research results . . . even providing videos.

For more information about the NASA STI Program Office, see the following:

- Access the NASA STI Program Home Page at ***http://www.sti.nasa.gov***

- E-mail your question via the Internet to help@sti.nasa.gov

- Fax your question to the NASA Access Help Desk at 301–621–0134

- Telephone the NASA Access Help Desk at 301–621–0390

- Write to:
  NASA Access Help Desk
  NASA Center for AeroSpace Information
  7121 Standard Drive
  Hanover, MD 21076

NASA/CR—2003-212311

Inflow/Outflow Conditions for Unsteady Aerodynamics and Aeroacoustics in Nonuniform Flow

Oliver V. Atassi
Pratt & Whitney, East Hartford, Connecticut

Prepared under Contract NAS3–12310

National Aeronautics and
Space Administration

Glenn Research Center

December 2003

Acknowledgments

The author would like to thank Professor H.M. Atassi and his students, Amr Au and Basman Hadidi for their help and collaboration on this project. Much of this work builds upon and uses the work they have done in this area over the last several years. The author would also like to thank Dr. Wesley Lord for his suggestion to generalize this work to mean flows with arbitrary radial distributions. Finally, the author would like to thank Dennis Huff as contract monitor for his steadfast support of this work.

Available from

NASA Center for Aerospace Information
7121 Standard Drive
Hanover, MD 21076

National Technical Information Service
5285 Port Royal Road
Springfield, VA 22100

Available electronically at http://gltrs.grc.nasa.gov

INFLOW/OUTFLOW CONDITIONS FOR UNSTEADY AERODYNAMICS AND AEROACOUSTICS IN NONUNIFORM FLOW

Oliver V. Atassi
Research Engineer
Pratt & Whitney

CONTRACT REPORT DRAFT

Abstract

The effect of a nonuniform mean flow on (i) the normal modes, (ii) the inflow/outflow nonreflecting boundary conditions, and (iii) the sound power are studied. The normal modes in an annular duct are computed using a spectral method in combination with a shooting method. The swirl causes force imbalance which couples the acoustic and vortical modes. The acoustic modes are distinguished from the vortical modes by their large pressure and small vorticity content. The mean swirl also produces a Doppler shift in frequency. This results in more counter-spinning modes cut-on at a given frequency than modes spinning with the swirl. Nonreflecting boundary conditions are formulated using the normal mode solutions. The inflow/outflow boundary conditions are implemented in a linearized Euler scheme and validated by computing the propagation of acoustic and vortical waves in a duct for a variety of swirling mean flows. Numerical results show that the evolution of the vortical disturbances is sensitive to the inflow conditions and the details of the wake excitations. All three components of the wake velocity must be considered to correctly compute the wake evolution and the blade upwash. For high frequencies, the acoustic-vortical mode coupling is weak and a conservation equation for the acoustic energy can be derived. Sound power calculations show significant mean flow swirl effects, but mode interference effects are small.

Contents

List of Tables

List of Figures

1 Introduction

Wakes shed from a fan interact with downstream lying guide vanes and struts to produce fan interaction noise. For tonal interaction noise, the harmonic content of the wakes are steady in a reference frame moving with the fan but in the absolute reference frame of the exit guide vanes, the wakes appear as unsteady disturbances rotating with the blade passing frequency of the fan. Our ability to directly compute this unsteady interaction is hindered by mathematical and numerical difficulties as well as by the computational intensiveness of the problem. A common approach is to limit the size of the computational domain and to confine the calculations to a single blade row. The mathematical formulation of the problem requires that the inflow and outflow conditions be defined accurately so as to represent both the wake harmonics and the upstream/downstream propagating acoustic waves. Moreover, causality imposes that a computational domain enclosing the noise source cannot have energy propagating into the domain from the inflow/outflow boundaries. This is accomplished by imposing nonreflecting inflow/outflow conditions. Since the radiated acoustic energy is a very small fraction of the total flow energy, a highly accurate procedure for simulating the noise generation mechanism and the propagation of sound must be developed.

In fan tonal interaction noise, the stator is the isolated blade row. In Figure 1, results from a Reynolds Averaged Navier-Stokes calculation for a representative fan design are given for the circumferentially averaged mean flow at the inflow plane lying between the fan and the stator. In the top figures, the radial profile of the total enthalpy and axial velocity are plotted from hub to tip and in the bottom figures the swirl velocity and total velocity distribution are plotted from hub to tip. The results show that the mean flow variables are nonuniform exhibiting three-dimensional effects with significant swirl velocity. The radial variations result mainly from nonuniform blade loading on the fan and viscous effects near the hub and tip. An accurate aerodynamic/aeroacoustic computational scheme must incorporate upstream and downstream mean flow nonuniformity effects. In particular, inflow/outflow conditions must be derived for flows with mean swirl and radial variations. This is increasingly important as fan and exit guide vane designs incorporate sweep and lean. The main objective of this work is to develop exact nonreflecting inflow/outflow conditions for nonuniform mean flows and to implement these conditions for aerodynamic/aeroacoustic calculations in an annular duct geometry.

Traditionally [1, 2, 3, 4], unsteady linearized Euler algorithms assume uniform mean flow conditions at the inflow and outflow boundaries. In this case, it is possible to express impinging disturbances as a superposition of acoustic, entropic and vortical modes obeying distinct equations [5]. Such approaches have been successfully applied to two dimensional and three dimensional problems with uniform mean flows.

For swirling mean flows, centrifugal and Coriolis effects produce force imbalance and, as a result, the acoustic, vortical and entropic modes are coupled [6, 7]. Moreover, the eigenvalue problem resulting from the normal mode analysis is not self-adjoint and, as a result, the modes may not form a complete set. Another consequence of the force imbalance is the development of a singular critical layer for the vortical modes, where it is very difficult to obtain accurate numerical solutions. To overcome this difficulty, the normal mode representation is limited to the acoustic pressure-dominated modes which propagate with a phase velocity equal to or larger than the local speed of sound in a reference frame moving with the local mean velocity [8]. In order to obtain a complete representation of the disturbance field, an initial-value-analysis is used to determine the vorticity and entropy-dominated fields which propagate with phase velocities close to the mean flow velocity. An iterative scheme which enforces conservation of mass momentum and energy is then used to ensure that the superposition of the nearly sonic and nearly convected fields exactly satisfy the Euler equations.

In section 2, we present a normal mode analysis to represent the acoustic modes in an annular duct and a criterion based on group velocity is used to satisfy the causality condition. In section 3, we present an iterative scheme for the inflow/outflow conditions and implement this scheme in an Euler code. The boundary conditions are then tested on the propagation of harmonic disturbances from an upstream imposed source in an annular duct with swirling mean flow. In section 4, an expression for the sound power in swirling flows is derived which may be used as a conservation law and to study the effect of mean swirl on the sound power.

2 Normal Mode Analysis in Nonuniform Swirling Flows

This section presents the normal mode analysis of the linearized Euler equations for nonuniform mean flows. The outgoing acoustic modes are used in the next section to formulate and implement nonreflecting boundary conditions.

2.1 Introduction

Sound propagating in a duct is usually expressed in terms of the duct normal modes. A major advantage is that at a given frequency, there are only a finite number of propagating modes. In aeroacoustic computations, the modes can also be used to derive exact expressions for the nonreflecting inlet/outlet boundary conditions.

As mentioned earlier, the mean flow velocity of fan engines is characterized by significant swirl and radial variations in both the axial and swirl components. Moreover, the work done by the upstream fan blades produces radial variations in the flow enthalpy, and losses in the boundary layers near the hub and tip walls produce significant changes in the entropy. Representative results from a Reynolds averaged Navier Stokes calculation are shown in Figure (1) for the circumferentially averaged total enthalpy variations downstream of the fan. Note the large rise in the total enthalpy in the tip region. This rise is associated with the tip vortex which is shed downstream of the fan.

Current fan noise schemes compute the wave modes in a constant area annular duct by assuming the mean flow is axial and uniform [9] or that the annulus is narrow [10, 11].The normal mode analysis can then be used to determine stator vane counts which cut-off blade passing frequency tone noise [12].

In order to incorporate nonuniform mean flow effects, a normal mode analysis of such flows must be carried out. Recent studies, to account for swirl, have assumed simple analytic models for the mean flow swirl which consist of combinations of free vortex and rigid body swirl [13, 14, 15]. These treatments assume uniform total enthalpy and entropy. The results show that the centrifugal and coriolis effects create force imbalances which couple the acoustic, vortical and entropic flow disturbances. However for the high frequencies relevant to fan tone noise, the coupling is weak ([14],[8]), *i.e.* the acoustic modes have small vorticity content and the vortical modes have small pressure content.

Another important application of the normal mode analysis is the formulation of nonreflecting boundary conditions. This, however, requires an accurate solution of the wave modes in a duct [3]. To examine the sensitivity of aeroacoustic computations to the accuracy of the acoustic modes used in the formulation of the nonreflecting boundary conditions, we consider the case of , a one-dimensional incident acoustic wave whose pressure is of the form $e^{i(kx-\omega t)}$ with an imposed outlet boundary condition error in the mode wavenumber, Δk. The solution is given by,

$$u(x,t) = [e^{ikx} + \frac{\sin(kx)}{\sin(kL)} e^{ikL}(i\Delta kL + O(\Delta kL)^2)]e^{-i\omega t}. \tag{1}$$

Note that the error in the numerical solution is linearly proportional to the error in the downstream boundary condition, Δk. Moreover, the error becomes very significant if the duct length is an integer multiple of $\lambda/2$.

Figure (2) shows the numerical solution and error in a domain of length .75 which is discretized with 33 points. The real part of the numerical solution is shown in the bottom plot of Figure (2) for various boundary condition errors, $\Delta k = 0.0, 0.025, 0.05, 0.1$, on the wavenumber, $k = 2\pi$. The relative error of the solution is shown in the top plot in Figure (2). Note the relative error of the numerical solution is directly proportional to the error at the exit boundary. For example, as the exit boundary condition error increases from .025 to .05 the relative error of the numerical solution increases from nearly .11 to .22. This degradation of the solution is visible in the solution where the exact solution is the solid black line. As the boundary condition error increases, modifications to both the phase and amplitude of the numerical solution are visible across the entire domain. The apparently small error right at the exit boundary, as is indicated by the small difference between the exact solution and the numerical solution at the end of the domain, is because we have plotted the real part of the solution and Δk is relatively small. This simple result highlights the importance of accurately specifying the exit boundary condition for general axisymmetric mean flow to obtain an accurate numerical solution.

In what follows, we (i) generalize the duct mode calculation for axisymmetric mean flow to allow arbitrary radial distributions, (ii) examine the effects of arbritrary swirl and enthalpy on the acoustic modes in a duct and (iii) compare this with the uniform flow, narrow annulus and uniform enthalpy models which have been used in earlier work. Many of the Results for the normal modes with arbitrary radial distributions are also in Ali et al [16].

2.2 Mathematical Formulation

For a non-viscous, non-heat-conducting perfect gas with constant specific heats, the governing equations are the Euler Equations,

$$\begin{aligned} \frac{D}{Dt}\vec{U} + \vec{U}\cdot\nabla\vec{U} &= \frac{-1}{\rho}\nabla p \\ \frac{D}{Dt}s &= 0. \end{aligned} \tag{2}$$

The flow variables are decomposed in terms of the sum between their steady mean values and their unsteady perturbations,

$$\vec{U}(\mathbf{x},t) = \vec{U}_0(\mathbf{x}) + \vec{u}(\vec{x},t), \tag{3}$$

$$p(\vec{x},t) = p_0(\vec{x}) + p'(\vec{x},t) \tag{4}$$

$$\rho(\vec{x},t) = \rho_0(\vec{x}) + \rho'(\vec{x},t), \tag{5}$$

$$s(\vec{x},t) = S_0(\mathbf{x}) + s'(\vec{x},t), \tag{6}$$

where $\vec{x}$ represents any coordinate system, $\vec{U}_0$, p_0, ρ_0, S_0 are the steady mean velocity, pressure, density and entropy, respectively, and $\vec{u}$, p', ρ', s' are the corresponding unsteady perturbation quantities. The unsteady quantities are assumed to be small such that $|\vec{u}(\vec{x},t)|, |p'|, |\rho'|, |s'| \ll \vec{U}_0(\vec{x}), p_0, \rho_0, S_0$. We non-dimensionalize with respect to the mean radius of the duct, r_m, and the mean density, ρ_m, and speed of sound, c_m, at the mean radius.

Substituting into (2), the nondimensional Euler equationsg reduce to the following coupled system of linear equations,

$$\frac{D_0}{Dt}[\vec{u} - s'/(2c_p)\vec{U}_0] + [(\vec{u} - s'/(2c_p)\vec{U}_0)\cdot\nabla]\vec{U}_0 = -\frac{p_0^{1/\gamma}}{\rho_0}\nabla(\frac{p'}{p_0^{1/\gamma}}), \tag{7}$$

$$\frac{D_0}{Dt}[\frac{p'}{\rho_0 c_0^2} - s'/(2c_p)] = -\frac{1}{\rho_0}\nabla\cdot(\rho_0\vec{u}), \tag{8}$$

$$\frac{D_0}{Dt}s' + \vec{u} \cdot \nabla S_0 = 0, \tag{9}$$

where $\frac{D_0}{Dt}$ is the mean flow material derivative

$$\frac{D_0}{Dt} \equiv \frac{\partial}{\partial t} + \vec{U}_0 \cdot \nabla. \tag{10}$$

The impermeablity condition is imposed at the hub and tip radii,

$$u_r = 0. \tag{11}$$

2.3 Mean Flow

The mean flow is assumed axisymmetric and, away from the upstream and downstream blade rows, the axial mean flow gradients are treated as much smaller than the radial gradients. In such a flow region, mass conservation implies that the radial velocity is small and the nondimensional mean flow velocity can be expressed in the form,

$$\vec{U}_0(\vec{x}) = M_x(r)\mathbf{e}_x + M_s(r)\mathbf{e}_\theta, \tag{12}$$

where $\mathbf{e}_x$ and $\mathbf{e}_\theta$ represent unit vectors in the axial and circumferential directions, respectively and $M_x(r) = U_x/c_m$ and $M_s(r) = U_s/c_m$. The mean flow is, in general, vortical with vorticity given by

$$\vec{\zeta}_0 = \nabla \times \vec{U}_0 = \frac{1}{r}\frac{d(rM_s)}{dr}\mathbf{e}_x - \frac{dM_x}{dr}\mathbf{e}_\theta. \tag{13}$$

The stagnation enthalpy, entropy, velocity, and vorticity are related by Crocco's equation

$$\nabla H = T\nabla S_0 + \vec{U}_0 \times \vec{\zeta}_0. \tag{14}$$

In order to study the effect of the mean flow on the eigenmodes in an annular duct with swirling flow and to test the robustness of the current scheme, two mean flows are used:

a) Theoretical Model represented by a combination of rigid body and free vortex swirl,

$$M_s = M_\Omega + M_\Gamma \tag{15}$$

where $M_\omega \; \alpha \; r$ and $M_\Gamma \; \alpha \; 1/r$. Assuming uniform enthalpy from hub to tip and an isentropic flow, the axial component of velocity takes the form,

$$M_x^2 = M_{xm}^2 - 2[\Omega^2(r^2 - 1) + 2\Omega\Gamma \ln(r)], \tag{16}$$

where M_{xm} is the axial Mach number at the mean radius of the duct.

b) Mean flow data from a fan design.

Mean flow data representative of a fan design [17] is compared to the first theoretical mean flow model. Figure (3-a) shows the total temperature which is proportional to the stagnation enthalpy across the annulus. For this fan design, the stagnation enthalpy is not constant but it varies 8% from hub to tip while the theoretical model gives constant stagnation temperature. Figure (3-b) shows the swirling component of the mean flow data along with the best fit of equation 15. Using the least square method, $M_{\Omega_m} = 0.2108$ and $M_{\Gamma_m} = 0.2498$. In figure (3-c), the axial component of the mean flow data is compared to the values obtained from equation (16). The figure shows a maximum difference of 15% between the two curves.

2.4 Normal Mode Expansion

Normal mode analysis is used to obtain the spectrum of propagating and evanescent acoustic-vorticity modes for the swirling flow equations. The following Fourier expansion is assumed

$$\begin{aligned}\{u_x, u_r, u_\theta, p', s'\}(x, r, \theta; t) &= \int_{-\infty}^{\infty} \sum_{m=-\infty}^{\infty} \sum_{n=1}^{\infty} \{X_{mn}(r), R_{mn}(r), \\ &\qquad T_{mn}(r), p_{mn}(r), s_{mn}(r)\} \times e^{i(-\omega t + m\theta + k_{mn} x)} d\omega, \qquad (17)\end{aligned}$$

where m, and n are integer modal numbers characterizing the circumferential and radial eigenmodes, respectively. Since the equations are linear, each Fourier component can be considered /eparately. The coupled system of equations (7,8) and (9) can now be represented in terms of normal modes as

$$\Lambda_{mn}(X_{mn} - \frac{M_x}{2c_p} s_{mn}) + \frac{dM_x}{dr}(-iR_{mn}) = -k_{mn}(\frac{1}{\rho_0} p_{mn}), \qquad (18)$$

$$i\Lambda_{mn} R_{mn} + \frac{M_s^2}{2c_p r} s_{mn} - \frac{2M_s}{r} T_{mn} + \frac{1}{\rho_0}\frac{dp_{mn}}{dr} - \frac{\frac{d\rho_0}{dr}}{(\gamma\rho_0 p_0)} p_{mn} = 0, \qquad (19)$$

$$\Lambda_{mn}(T_{mn} - \frac{M_s}{2c_p} s_{mn}) + \frac{1}{r}\frac{d}{dr}(rM_s)(-iR_{mn}) + \frac{m}{\rho_0 r} p_{mn} = 0, \qquad (20)$$

$$\Lambda_{mn}(\frac{p_{mn}}{\rho_0 c_0^2} - s_{mn}/(2c_p)) + \frac{m}{r}T_{mn} + \frac{1}{\rho_0 r}\frac{d}{dr}[\rho_0 r](-iR_{mn}) + \frac{d}{dr}(-iR_{mn}) = k_{mn}X_{mn}, \quad (21)$$

$$s_{mn} = \frac{\frac{dS_0}{dr}}{\Lambda_{mn}} iR_{mn}, \quad (22)$$

where the convective eigenvalue, Λ_{mn}, is defined by the expression,

$$\Lambda_{mn} = -\omega + k_{mn}M_x + \frac{mM_s}{r}. \quad (23)$$

The boundary condition at the hub and tip radii is

$$R_{mn}(r) = 0. \quad (24)$$

Note that unlike the uniform axial mean flow limit this is not a Sturm-Liouville eigenvalue problem. Therefore there is no proof of completeness or orthogonality of the eigenfunctions.

2.5 Numerical Methods

A combination of a pseudo-spectral method and a shooting method is used in order to obtain the eigenmodes and eliminate any spurious modes. In the pseudo-spectral method, the eigenfunctions are represented by a series of Chebyshev polynomials which form a complete orthogonal set [14].

For an annular duct, the physical domain $r_h \le r \le r_t$ is mapped to $-1 \le x \le 1$. Choosing the grid points as $x_l = \cos[\pi(l-1)/(N-1)]$ for $1 \le l \le N$, the eigenfunctions can be represented as,

$$f_l = \sum_{p=1}^{N} a_p \cos[\pi(p-1)(l-1)/(N-1)], \quad (25)$$

where a_p are coefficients of the spectral expansion. Derivatives then are given by $f_l' = W_{jl}^{(1)} f_j$ and $f_l'' = W_{jl}^{(2)} f_j$, where $W_{jl}^{(1)}$ and $W_{jl}^{(2)}$ are known coefficient matrices [18].

The problem is reduced to solving an algebraic eigensystem of the form,

$$[A]\mathbf{x} = k_{mn}[B]\mathbf{x} \quad (26)$$

where the matrices $[A]$ and $[B]$ result from equations (18-21) after discretization and **x** is a vector of the eigenfunctions X_{mn}, p_{mn}, R_{mn}, and T_{mn}. The algebraic eigensystem is then solved by a shifted QR algorithm [19].

This method has exponential convergence and can resolve thin layers of steep changes. The disadvantage of this method is that the matrices $[A]$ and $[B]$ are usually not sparse which may lead to difficulties in solving the eigensystem as the number of grid points increases. It also has the disadvantage, like the finite difference method, that this system of $4N$ equations has $4N$ solutions. Since the number of physical solutions in a problem is independent of the numerical grid, the vast majority of these solutions are spurious.

An alternative method to solve the eigenvalue problem is the shooting method. In this method, equations (18-21) are cast in the following form,

$$\frac{d}{dr}\mathbf{Y} = F(\mathbf{Y}). \tag{27}$$

In the present problem, $Y = \{p_{mn}, -iR_{mn}\}^T$, and equation (27) becomes,

$$\frac{dp_{mn}}{dr} = \rho_0(-i\Lambda_{mn}R_{mn} - \frac{M_s^2}{2c_p r}s_{mn} + 2\frac{M_s}{r}T_{mn}) + \frac{\frac{dp_0}{dr}}{(\gamma p_0)}p_{mn} \tag{28}$$

$$\frac{d(-iR_{mn})}{dr} = -\Lambda_{mn}(\frac{p_{mn}}{\rho_0 c_0^2} - \frac{s_{mn}}{c_p}) - \frac{m}{r}T_{mn} + k_{mn}X_{mn} + \frac{\frac{d(r\rho_0)}{dr}}{\rho_0 r}(iR_{mn}). \tag{29}$$

The axial and tangential velocity components T_{mn}, X_{mn} are functions of p_{mn} and R_{mn},

$$T_{mn} = \frac{1}{\Lambda_{mn}}[(iR_{mn})\frac{1}{r}\frac{d}{dr}(rM_s) - \frac{m}{\rho_0 r}p_{mn}] + \frac{M_s}{2c_p}s_{mn}, \tag{30}$$

$$X_{mn} = \frac{1}{\Lambda_{mn}}[\frac{dM_x}{dr}(iR_{mn}) - \frac{k_{mn}}{\rho_0}p_{mn} + k_{mn}\frac{M_x^2}{2c_p}s_{mn}] + \frac{M_x}{2c_p}s_{mn} \tag{31}$$

and s_{mn} is determined from (22).

The initial conditions at r_h are given and assuming an initial guess for k_{mn}, the previous equations are integrated using a Runge-Kutta scheme from r_h to r_t. The boundary condition at r_t is checked. If this boundary condition is not satisfied, another value of k_{mn} is assumed until the boundary condition at r_t is satisfied. Newton method or secant method is used for the iteration process of k_{mn}. The main advantage of the shooting method over the finite difference and spectral method is that it does not produce spurious modes. However, it needs an initial guess for each eigenvalue which makes it impossible to cover all the eigenvalues in the complex plane. Also, it may not directly yield solutions with discontinuity or very steep gradients. In the present work, we use a combination of the pseudo-spectral method and a shooting method. The pseudo-spectral method provides the initial guess for the shooting method which eliminates the spurious modes and improves the accuracy of the solution.

Figure (4) shows a comparison of the eigenmode spectra obtained by the pseudo-spectral method and that obtained by the shooting method for a case of $m = -1$ and $\omega = 16$ using the isentropic mean flow data in figure (3). The vertical axis corresponds to the imaginary part of the axial wavenumber and the horizontal axis corresponds to the real part. Those modes which lie on the horizontal line corresponding to zero imaginary part represent unsteady disturbances which propagate downstream without decay. The modes with positive imaginary part correspond to evanescent modes. A typical eigenmode spectrum for swirling flows consists of two families of solutions. The first family represent the pressure-dominated modes, herein referred to as the acoustic modes, and consists of propagating modes and evanescent modes. This family appears on the left side of figure (4). The other family consists of vortical modes and appears on the right side of figure (4). A calculation of the group velocity shows that the acoustic modes to the left of the evanescent modes propagate upstream and the acoustic modes to the right of the evanescent modes propagate downstream. The group velocity was calculated numerically since there is no closed form expression for it. In figure (4), two of the acoustic propagating modes obtained by the pseudo-spectral method are spurious; one of them appears to propagate upstream and the other appears to propagate downstream. However, using these eigenvalues as initial guesses for the shooting method results in a single acoustic mode. Some of the evanescent modes of the pseudo-spectral method also are inaccurate. It is difficult to assert using the shooting method whether the nearly convected modes are spurious or not. This is due to the singular behavior of the eigensolutions at certain values of the radius. However, due to the singular behavior of the eigensolutions in the critical layer an initial value approach is derived in section 3 to completely represent the non-acoustic disturbances for the inflow/outflow boundary conditions. In section 2.6, we compare our eigenvalue algorithm against the narrow annulus limit and the uniform enthalpy limit to assess the range of validity of these cases.

2.6 Narrow Annulus Limit

In the narrow annulus limit, analytic expressions for the dispersion relation and radial eigenfunctions can be derived. In order to examine the accuracy of the present model and assess the limitations of the narrow annulus model, we briefly present the dispersion relation and eigenfunctions of the acoustic modes in the narrow annulus limit and compare the number of propagating modes and the radial eigenfunctions obtained analytically with those determined from computation of the general problem.

Since the annulus is assumed narrow, i.e. $r_h/r_t << 1$, we can expand the radius, mean velocity, density, pressure and speed of sound about the mean radius in terms of a perturbation expansion of the form,

$$\begin{aligned} r &= 1 + \epsilon\tilde{r} + \cdots \\ \vec{U}_0 &= M_x(1)\hat{e}_x + M_\theta(1)\hat{e}_\theta + O(\epsilon) \\ (\rho_0, p_0, c_0) &= (1, p_0, 1) + O(\epsilon) \end{aligned} \tag{32}$$

where $|\epsilon| << 1$. As a result, the leading order mean flow quantities are uniform. In this limit, the linearized Euler equations become,

$$\frac{D_0^2 p'}{Dt^2} - \nabla^2 p' = 0 \tag{33}$$

where $\frac{D_0}{Dt} = \frac{\partial}{\partial t} + M_x\frac{\partial}{\partial x} + M_s\frac{\partial}{\partial \theta}$. To satisfy impermeability at the hub and tip, we impose

$$\frac{\partial p'}{\partial r} = 0, \qquad r = r_h, r_t. \tag{34}$$

Solutions to (33, 34) exist of the form,

$$p' = \sum_{m=-\infty}^{m=\infty} \sum_{n=1}^{n=\infty} \cos[\gamma_{mn}(r - r_h)]e^{i(m\theta + k_{mn}x - \omega t)} \tag{35}$$

where

$$k_{mn} = \frac{-\tilde{\omega}M_x \pm \sqrt{\tilde{\omega}^2 - \beta^2(m^2 + \gamma_{mn}^2)}}{\beta^2} \tag{36}$$

with $\tilde{\omega} = \omega - mM_s$, $\beta = 1 - M_x^2$ and $\gamma_{mn} = \frac{n\pi}{(r_t - r_h)}$. Equation (36) indicates that the number of propagating modes depends upon the reduced frequency of the disturbance. The swirl component of velocity acts as a Doppler effect to increase the frequency if the disturbance is rotating in a direction counter to the swirl component and to decrease the frequency if the disturbance rotates in the same direction as the swirl. Moreover, the number of propagating modes grows with frequency. The analytical solution also indicates that if a radial mode is propagating at a given frequency, it will propagate at higher frequencies. As a result, one can determine all the radial modes at all frequencies by computing the radial modes at the maximum frequency of interest, $\tilde{\omega} = \tilde{\omega}_{max}$. In what follows, we examine solutions for both narrow the annullus and the general case to examine the extent to which the narrow annulus approximation is adequate for real three dimensional geometries.

2.7 RESULTS and DISCUSSION

In this section, we present the normal mode solutions for a variety of mean flows and hub-tip ratios. The eigenfunctions, p_{mn}, are normalized numerically such that the norm of each mode satisfies,

$$\int_{r_h}^{r_t} [r||p_{mn}||^2] dr = 1. \tag{37}$$

2.7.1 Effect of Hub-Tip Ratio and Frequency on Duct Modes

We examine the effect of hub-tip ratio and reduced frequency on the duct modes. For simplicity, we consider a mean flow with free vortex swirl and examine two cases. The problem is characterized by the parameters $\omega_r = \omega r_m/c_0$, $r^* = r_h/r_t$ and $\tilde{\Gamma} = \Gamma/(\omega r_m^2)$.

In case one, we consider a large spinning mode order, $m = -20$ with $\omega_r = 30$, $r^* = .4$ and $\tilde{\Gamma} = .21$. Figure (5), shows there are 6 downstream propagating radial eigenfunctions. Each radial mode is characterized by a different number of zero crossings. We note that the modes are quite different from the sinusoidal solution obtained by the analytic result. For example, the amplitude of the numerically determined eigenfunctions are strongly weighted in the hub region and only become sinusoidal in the tip region. This is not surprising since the hub-tip ratio for this case is outside the range where the narrow annulus solution would be expected to be valid.

In case two, we consider a smaller spinning mode order, $m = -1$, with $r^* = .4$ and $\tilde{\Gamma} = .21$ and compare the solutions for two different reduced frequencies, $\omega_r = 20, 40$. In figure (6), we plot the sixth radial mode for the two reduced frequencies taken in case two. Note that, as in the narrow annulus limit, the radial eigenfunctions are independent of the frequency.

2.7.2 Effect of Mean Flow Model

Figure 7 compares the eigenmodes obtained using the mean flow data and the theoretical mean flow model of equations (15) and (16) for $m = -12$ and $\omega = 24.2$. The number of acoustic propagating modes is six modes in each direction for the two swirling flow models. For the case of no swirl, the number of acoustic propagating modes does not change. The effect of the mean flow model on the downstream acoustic modes is small while the effect is more significant on the upstream acoustic modes. The strongest effect of the mean flow model is on the convected modes.

The effect of the mean flow model on the eigenfunctions of the six upstream acoustic propagating modes is shown in figure (8). The mean flow model has a significant effect on the eigenfunction radial variation. As the order of the mode increases this effect decreases.

The effect of the mean flow model on the eigenfunctions of the six downstream acoustic propagating modes is shown in figure (9). The effect of the mean flow model on these eigenfunctions is significant only for the first two modes. This result is not surprising since it is expected that the longer wavelength radial disturbances will be more influenced by the mean flow gradients which vary on the mean radius lengthscale than on the short wavelength higher order radial modes.

2.8 Summary

A numerical method was developed to compute the normal modes in an axisymmetric mean flow with arbitrary swirl. Two sets of propagating modes were found. One set is pressure-dominated and propagates with a phase velocity, in a reference frame moving with the mean velocity, greater than or equal to the local speed of sound. The other set propagates with a phase velocity close to the mean flow velocity. Numerical results were presented for a variety of mean flows and compared with the narrow annulus and uniform enthalpy limits to examine the importance of centrifugal effects and enthalpy variations on the acoustic modes. The results lead to the following conclusions. (i) The number of propagating modes is strongly dependent upon whether the modes are co-rotating or counter-rotating to the mean swirl due to the doppler shift in frequency. (ii) Mean flow swirl refraction effects are more important for the upstream-going modes than the downstream-going modes resulting in larger deviations in the eigenvalues of the upstream-going modes. This is because the upstream modes propagate with lower phase speeds, while the downstream modes propagate with higher phase speeds, and are thus less affected by the mean flow swirl velocity. (iii) The narrow annulus limit misses centrifugal effects which are important for moderate hub-tip ratios and as a result misses the behavior of the eigenfunctions in the hub region. (iv) The uniform enthalphy limit is a reasonable approximation for the higher order radial modes but is inaccurate for predicting the behavior of the lower order radial modes.

The generalized eigenvalue scheme presented is a necessary module of any computational acoustics scheme which employs nonreflecting boundary conditions. The coupling of this analysis to a numerical scheme is presented in section 3.

3 Boundary Conditions for Aerodynamic and Aeroacoustic Computations

3.1 Introduction

In this section, we derive time-harmonic inflow/outflow conditions for unsteady aerodynamic/aeroacoustic computations based on the linearized Euler equations. We first examine the results of a uniform mean flow which was treated and applied to various three-dimensional wake and acoustic wave excitations in [3]. In this case, at the inlet of the computational domain, the inflow conditions imposed an incident acoustic or vortical wave and applied a nonreflecting condition for the radiated pressure. At the outlet boundary, we specified two conditions: a nonreflecting boundary condition for the pressure and a pure convection condition for the vortical part of the velocity. The exact outlet conditions result from the property that in a uniform mean flow the acoustic, entropic and vortical disturbances can be split into distinct modes [5].

For mean flows with swirl, it is not possible to split the disturbances into distinct modes because the local Coriolis and centrifugal forces couple the various modes. Thus, as was shown in the previous section, there are pressure-dominated modes which mainly represent the acoustic part of the unsteady flow and vorticity-dominated modes propagating at nearly convected velocities. Moreover, there is an infinite number of vorticity-dominated modes which cluster at each side of the critical layer [7].

Montgomery et al. [4] attempted to circumvent this difficulty by approximating the vorticity-dominated disturbances as pressure-free convected disturbances. However, this representation does not satisfy the radial momentum equation in nonuniform flow. Golubev & Atassi [8, 20], used an initial-value analysis to represent the vortically-dominated disturbances and have combined this analysis with the normal mode analysis to develop accurate boundary conditions for high frequency, rigid body and free vortex swirling flows. Their results, along with Elhadidi et. al [21], show that the stability and growth of the vorticity-dominated modes depend on the mean flow swirl distribution and affects the upwash velocity along a blade surface.

In the present work, we extend the analysis of [8] to general swirling flows and present an algorithm for the boundary conditions which accounts for the coupling between the acoustic and vortical modes. We implement the boundary conditions in a linearized Euler solver and, as an application, we test the boundary conditions by computing the propagation of acoustic and vortical disturbances in an annular duct. Sensitivity of the solution to inflow conditions is examined and, in particular, the effect of representing the inflow excitation as a convected disturbance is studied.

In section 3.2, we derive nonreflecting inflow/outflow boundary conditions for swirling flows. The Euler scheme and the propagation of acoustic and vortical disturbances in an annular duct with nonuniform mean flow is presented in section 3.3. In section 3.4, we compute the propagation of vortical and acoustic waves in a variety of mean flows and examine the importance of the inflow wake specification on the evolution of the wake.

3.2 Nonreflecting Boundary Conditions

Based on the normal mode analysis in section 2, the pressure-dominated modes can be expressed in terms of the eigenfunction expansion,

$$p_s^+ = \sum_{m=-\infty}^{m=\infty} \sum_{n=1}^{n=\infty} a_{mn}^+ p_{mn}^+(r) e^{i(k_{mn}^+ x + m\theta - \omega t)}, \tag{38}$$

$$p_s^- = \sum_{m=-\infty}^{m=\infty} \sum_{n=1}^{n=\infty} a_{mn}^- p_{mn}^-(r) e^{i(k_{mn}^- x + m\theta - \omega t)} \tag{39}$$

where the + (−) indicates modes propagating with a group velocity downstream (upstream). Thus, p_s^+ corresponds to the sonic part of the pressure whose energy propagates downstream and p_s^- represents the acoustic pressure whose energy propagates upstream.

In order to avoid small terms in (38) which may cause numerical difficulties, we use a finite number of propagating and slowly decaying modes to represent the pressure. The series expansion can be truncated to a finite number of terms with negligible error. Discretizing and truncating the expansion so that there are N_r radial modes and N_θ circumferential modes we obtain,

$$p_{s_{jk}}^+(x_0, \theta_{jk}, r_{jk}, t) = \sum_{m=-N_\theta/2}^{m=N_\theta/2-1} \sum_{n=1}^{n=N_r} a_{mn}^+ p_{mn}^+(r_{jk}) e^{i(k_{mn}^+ x_0 + m\theta_{jk} - \omega t)}, \tag{40}$$

$$p_{s_{jk}}^-(x_0, \theta_{jk}, r_{jk}, t) = \sum_{m=-N_\theta/2}^{m=N_\theta/2-1} \sum_{n=1}^{n=N_r} a_{mn}^- p_{mn}^-(r_{jk}) e^{i(k_{mn}^- x_0 + m\theta_{jk} - \omega t)} \tag{41}$$

Note that $p_{s_{jk}}^\pm$ can be cast as a vector with values at each of the inlet plane points (θ_{jk}, r_{jk}) in the form,

$$\{p_{s_{jk}}^\pm\} = (M_{x_0}^\pm A^\pm) e^{-i\omega t}. \tag{42}$$

where $M_{x_0}^\pm$ are $N_r N_\theta \times N_r N_\theta$ square matrices containing the axial, circumferential and radial eignfunctions for each of the N_r radial modes and N_θ cicumferential modes. The amplitude vectors containing the amplitudes, $a_{mn}^\pm$, of the $N_r N_\theta$ modes is denoted by $A^\pm$. The pressure is evaluated at $N_r N_\theta$ points in the inlet/outlet plane. The indices j, k refer to the grid points in the axial plane, $x = x_0$, with $j = 1, 2, ..., N_\theta$ and $k = 1, 2, ..., N_r$.

3.2.1 Inflow Boundary Condition

The unsteady pressure, velocity and entropy can be expressed as the sum of an outgoing nearly sonic field and a known incident field which is some combination of acoustic and vortical waves,

$$p = p_s^- + p_s^I + p_c^I, \tag{43}$$

$$\vec{u} = \vec{u}_s^- + \vec{u}_s^I + \vec{u}_c^I, \tag{44}$$

$$s' = s_s^- + s_s^I + s_c^I. \tag{45}$$

We assume that the known incident field, $p^I = p_s^I + p_c^I, \vec{u}^I = \vec{u}_s^I + \vec{u}_c^I, s^I = s_s^I + s_c^I$, is obtained via experiment or computation. Given this information, we propose the following boundary condition at the inlet boundary.

Nonreflecting Boundary Condition Algorithm

1. The sonic incident field, p_s^I is obtained by projecting p^I onto the incoming normal duct modes. With p_s^I determined u_s^I and s_s^I are determined from the normal mode analysis given in section 2.

2. The nearly convected incident field is then given by $\vec{u}_c^I = \vec{u}^I - \vec{u}_s^I, p_c^I = p^I - p_s^I, s_c^I = s^I - s_s^I$.

3. The inlet condition for the upstream-going acoustic waves, p_s^-, is expressed

$$p_s^- = (p - p^I) = M_{x_0}^- M_{(x_0+\Delta x)}^{-^{-1}} (p - p^I)_{(x_0+\Delta x)}. \tag{46}$$

Given p_s^-, we can determine from the normal mode analysis, given in section 2, u_s^- and s_s^-.

3.2.2 Outflow Boundary Condition

At the outflow boundary, the unknown solution contains a superposition of outgoing acoustic and vortically-dominated disturbances,

$$\begin{aligned} p &= p_s^+ + p_c, \\ \vec{u} &= \vec{u}_s^+ + \vec{u}_c \\ s' &= s_s^+ + s_c. \end{aligned} \tag{47}$$

In contrast to the inlet boundary, the outlet boundary has two unknowns: the downstream-going acoustic waves and the downstream-going nearly convected disturbances. As a result, two conditions are needed to specify the outlet boundary condition. One for the outgoing acoustic waves and one for the outgoing nearly convected waves.

Nonreflecting Boundary Condition Algorithm

1. The exit condition, $x = x_{N_x}$, for the outgoing acoustic pressure waves is expressed by

$$p_s^+ = (p - p_c^{old}) = M_{x_{N_x}}^+ M_{(x_{N_x}-\Delta x)}^{+^{-1}} p_{s_{(x_{N_x}-\Delta x)}}^+ . \tag{48}$$

Initially, we set $p_c^{old} = 0$ implying $p_s^+ = p$. In later iterations, we express $p_s^+ = p - p_c^{old}$. Given p_s^+, we can determine from the normal mode relations in section 2 u_s^+ and s_s^+.

2. The nearly convected part of the solution is given by $\vec{u}_c = \vec{u} - \vec{u}_s^+, s_c = s' - s_s^+$. The new convected pressure field, p_c^{new}, is determined from using the mass and momentum equations (7,8). A condition of the form $\frac{D_0}{Dt}\vec{u}_c + \vec{u}_c \cdot \nabla \vec{U} = 0$ is applied on the convected velocity field.

3. Check $p_c^{new} - p_c^{old}$. If difference is greater than 1×10^{-2}, set $p_c^{old} = p_c^{new}$.

3.2.3 The High Frequency, Homentropic Limit

The exit boundary condition initially assumes that the nearly convected pressure field, p_c, is small and then iterates in time to reach a converged solution. In order to justify this initial guess, we consider the high frequency and homentropic, limit. In gust response applications, the reduced frequency is large and the radial entropy gradients are small except near the tip of the annulus where the tip vortex lies. In this limit, significant simplifications to the exit condition can be attained.

The vorticity-dominated disturbances are periodic over the upstream blade row passage and move with a phase velocity close to the mean flow velocity. Without loss of generality, these disturbances can be expanded in the form [8],

$$(\vec{u}^c, p^c, s^c) = \sum_{m=-\infty}^{m=\infty} \{\vec{A}_m(x,r), p_m^c(x,r), s_m^c(x,r)\} e^{i\phi_m}, \tag{49}$$

where $\phi_m = \alpha_m x + m\theta - \omega t$ is defined such that

$$\frac{D_0}{Dt}\phi_m \equiv 0, \tag{50}$$

and m is an integer index which for tone noise is a multiple of the number of blades upstream and $\vec{A}_m = (A_{mx}, A_{m\theta}, A_{mr})$. Equation (50) implies that

$$\alpha_m = \frac{(\omega - M_\theta m/r)}{M_x}. \tag{51}$$

In the high frequency limit, the gust disturbance scales with the blade passage lengthscale, $l_g = (2\pi r_m)/(m)$ and the mean flow variations scale with the mean radius. Typically, the number of fan blades is large implying that for tonal applications l_g/r_m is small, $O(\epsilon)$, and the reduced frequency, ω, is large, $O(1/\epsilon)$ where $\epsilon << 1$. We further assume that α_m is large from (51). In this case, the nearly convected disturbances propagate as slowly modulated wavetrains with rapidly varying phase. As a result, the leading order contributions to the Euler equations become,

$$(\frac{xr}{m}\frac{d}{dr}\alpha_m)A_{mr} + A_{m\theta} + \frac{\alpha_m r}{m}A_{mx} = 0, \tag{52}$$

$$M_x\frac{\partial A_{mx}}{\partial x} + \frac{dM_x}{dr}A_{mr} = -\frac{1}{\rho_0}(i\alpha_m p^c_m), \tag{53}$$

$$M_x\frac{\partial A_{m\theta}}{\partial x} + \frac{1}{r}\frac{d}{dr}(rM_\theta)A_{mr} = -\frac{1}{\rho_0}(\frac{imp^c_m}{r}), \tag{54}$$

$$M_x\frac{\partial A_{mr}}{\partial x} - 2\frac{M_\theta}{r}A_{m\theta} = -\frac{1}{\rho_0}\frac{d}{dr}\alpha_m(ixp^c_m) \tag{55}$$

where although α_m, m are large $(\alpha_m p^c_m)$ and (mp^c_m) are $O(1)$. This implies that in the high frequency limit, p^c_m is $O(\epsilon)$. Note that even in the case where only α_m or m is large p^c_m is $O(\epsilon)$. As a result, the pressure field associated with the vortically-dominated disturbances is small and the pressure is to leading order determined from the sonic pressure, p^s. Thus, in the high frequency limit, the corrections to the pressure field resulting from the iterative process are small and the vortical and acoustic disturbances are uncoupled. This result suggests that the exit boundary condition can be satisfied to leading order with only one interation.

3.3 Wake Excitation

In this section, we calculate the wake excitation from the rotor-locked flow field. In previous work [4], experimental data was taken for only two components of the velocity and so at the inflow the wake was modeled as a convected disturbance with zero radial velocity and pressure. Such an inflow specification does not satisfy the linearized radial momentum equation. Moreover, the second blade passing Fourier component of the rotor locked field shown in figure (15) shows that the velocity field is fully three dimensional with a significant radial velocity component. In order to uniquely specify the wake four of the five (three of the four for homentropic flow) flow variables must be measured or computed via a CFD calculation of the fan to uniquely specify the inflow source, $\vec{u}^I, p^I$ and s^I. The unknown component can then be determined from the continuity equation.

To determine the inflow excitation, the rotor-locked flow velocity far downstream of the upstream blade row is assumed periodic over the passage of the upstream blade row. As a result, the flow variables can be expanded in a Fourier series,

$$\begin{aligned}
\vec{u}^I &= \sum_{m=-\infty}^{m=\infty} \vec{u}^I_m e^{-imN_b\theta} \\
p^I &= \sum_{m=-\infty}^{m=\infty} p^I_m e^{-imN_b\theta} \\
s^I &= \sum_{m=-\infty}^{m=\infty} s^I_m e^{-imN_b\theta}
\end{aligned} \tag{56}$$

where the Fourier coefficients are given by

$$\begin{aligned}
\vec{u}^I_m &= \frac{N_b}{2\pi}\int_\theta^{\theta+\frac{2\pi}{N_b}} \vec{u}^I e^{imN_b\theta'} d\theta' \\
p^I_m &= \frac{N_b}{2\pi}\int_\theta^{\theta+\frac{2\pi}{N_b}} p^I e^{imN_b\theta'} d\theta' \\
s^I_m &= \frac{N_b}{2\pi}\int_\theta^{\theta+\frac{2\pi}{N_b}} s^I e^{imN_b\theta'} d\theta'.
\end{aligned} \tag{57}$$

The flow variables $\vec{u}^I, p^I, s^I$ can be determined from Reynolds averaged Navier-Stokes calculation or experiment. For fan applications, the entropy variation is typically small except in the tip regions. As a result, the inflow plane may be assumed homentropic and only three components of the velocity need to be computed or measured.

3.4 Numerical Formulation for the Interior Domain

In this section, we assume the flow to be governed by the linearized Euler equations (7, 8, 9) and we briefly present the interior Euler scheme for computing the propagation of acoustic and vortical disturbances in a duct. This model problem enables us to examine the convergence and accuracy of the numerical solution and assess the accuracy of the nonreflecting boundary conditions. The characteristic lengthscale, $L = r_m$, is taken to be the mean radius of the annulus. Nondimensionalizing, assuming solutions of the form $V = U(\vec{x}, t)e^{-i\omega t}$, the linearized Euler equations can be expressed

$$\mathcal{L}U = -\frac{\partial U}{\partial t}, \tag{58}$$

where $U = [\hat{\rho}, \hat{u}_x, \hat{u}_\theta, \hat{u}_r, \hat{s}]^T$, $\mathcal{L} \equiv -\mathbf{I}(i\omega) + \mathbf{A_x}\frac{\partial}{\partial x} + \frac{\mathbf{B}_\theta}{r}\frac{\partial}{\partial \theta} + \mathbf{C}_r\frac{\partial}{\partial r} + \frac{\mathbf{D}}{r}$. The variable coefficients $\mathbf{A_x} - \mathbf{D}$ depend upon the mean flow and the mean flow gradients. Equation (58) is discretized with a second order accurate Lax Wendroff scheme. Note that although the problem is time-harmonic, the time derivative remains and represents whatever transient time-dependence exists from the initial condition. The term $\frac{\partial U}{\partial t}$ or residual is used to denote that the numerical solution iterates in time to a steady state solution. Hence, when $\frac{\partial U}{\partial t} \to 0$ a steady state solution is obtained consisting of a single frequency, ω. The impermeability condition at the hub, $r = r_h/r_t$, and the tip, $r = 1$, of the annulus imply

$$\hat{u}_r(x, \theta, r_h/r_t) = \hat{u}_r(x, \theta, 1) = 0. \tag{59}$$

To relate this model problem to harmonic rotor-stator interaction whereby an upstream rotor consisting of N_b blades interacts with a stator consisting of N_v structural vanes, the solution is assumed quasi-periodic in θ. In this case, the computational domain extends from $[0, 2\pi/N_v]$. Quasi-periodicity implies $U(x, 0, r) = U(x, 2\pi/N_v, r)e^{i\sigma}$ where $\sigma = 2\pi n N_b/N_v$ with n being the harmonic of the upstream excitation. To complete the formulation of this initial-boundary-value problem, nonreflecting boundary conditions, as described in section 3.3, are imposed at the inflow and outflow boundaries of the computational domain.

3.5 Numerical Results

The Euler scheme is applied to compute the propagation of acoustic and vortical waves for a variety of mean flows ranging from uniform mean flow to simple swirling flows consisting of some combination of free vortex and rigid body swirl. We also consider a variety of inflow excitations ranging from an acoustic excitation to a vortical excitation to a combination of the two. Since there is no scattering body, no reflected waves should reach the upstream boundary. The upstream nonreflecting boundary condition is then,

$$U(0,\theta,r) = U^I(0,\theta,r). \tag{60}$$

3.5.1 Uniform Mean Flow

The uniform flow test case is motivated by the problem proposed by the CAA workshop [22]. An incident wave consisting of both a vortical transverse disturbance and a pressure disturbance is imposed for various hub-tip ratios and radial phase variations. The incident disturbance is,

$$U^I = A(r)e^{im\theta} + B(r)e^{i[N_b\theta + 2\pi q(\frac{r-r_h}{r_t-r_h})]} \tag{61}$$

where $A(r)$ is the amplitude vector of the acoustic disturbance and $B(r)$ is the amplitude vector of the vortical disturbance. The amplitude of the incident disturbance is given by

$$\begin{aligned} A^T &= [i(\omega - M_x k^+_{mn})p^+_{mn}, ik^+_{mn}p^+_{mn}, (im/r)p^+_{mn}, \frac{d}{dr}p_{mn}], \\ B^T &= \kappa[0, \frac{-M_x N_b}{\omega r}, 1, 0] \end{aligned} \tag{62}$$

where κ is used to indicate the size of the vortical disturbance relative to the acoustic disturbance. The parameters q and r_h/r_t give the degree of radial phase variation in the vortical gust. The outflow boundary condition (46) is used for the remainder of the infinite domain. Note that in the uniform flow limit one only needs to express a condition for the pressure [3] since the acoustic and vortical fields are decoupled. For simplicity, a uniform grid is used to study the convergence of the fully three-dimensional case. The range of parameters studied in the five cases are shown in table 1. To obtain a measure of the convergence of the scheme and its evolution to a steady state the average relative error,

$$\bar{E} = \sum_{i=1}^{N} \frac{||U^i_e - U^i_n||}{||U^i_e||} / (N) \tag{63}$$

is computed at each timestep where N is the total number of points in the domain and i is the grid index. Upstream, we impose a disturbance, $U^I(0,\theta)$. From the normal mode analysis the 'exact' solution, U_e, can be obtained. We consider five cases to study how well the numerical solution converges for problems with varying degrees of three-dimensionality. The radial phase of the gust is the parameter which governs the strength of the radial

Parameters	Case I	Case II	Case III	Case IV	Case V
$\omega L/c$	2π	2π	2π	2π	2π
σ	$4\pi/3.$	$4\pi/3$	$4\pi/3$	$4\pi/3$	$4\pi/3$
M_x	.5	.5	.5	.5	.5
r_h/r_t	.65	.65	.65	.65	.65
q	1/4	1/2	1	1	2
κ	.1	.1	.1	1	1

Table 1: Selected parameters for five cases of wave propagation in a uniform mean flow.

variation in each case. The parameters, q and κ are varied, while the other parameters are held constant in cases I-V as shown in table 2. In each case, the variables $(\hat{\rho}, \hat{u}_\theta, \hat{u}_r)$ are plotted against x, θ and r respectively and the global relative error of the density is plotted versus time iteration. In Figures 10, 11 and 12, the solution and the relative error are plotted for cases I, II and III. The grid in all the cases considered is $80 \times 25 \times 20$ in x, θ and r, respectively. The dashed lines correspond to the exact solution and the solid lines correspond to the numerical solution. The agreement is quite good and the relative error of the density is .1 percent when the solution reaches a steady state. In this case, $q = 1/4, 1/2, 1$ with $\kappa = .1$ and the increasing variation in r is most observable in the plot of u_θ versus r.

In Figures 13 and 14, the solution and the relative error are plotted for cases IV and V. In both these cases, the agreement with the exact solution is quite good and the relative error of the density is approximately .1 percent. In both these cases, the radial variation is more pronounced $q = 1, 2$, $r_h/r_t = .65$ and $\kappa = 1$, respectively. Note to more clearly demonstrate the radial variation, we have set the amplitude of the vortical waves to be ten times what they were in Figures 10-12.

The amount of transient noise in the solution is very small as is observable from the small oscillations in the relative error versus iteration plots. The effect of these transients on the computed solution is not discernible in the physical solution.

3.5.2 Acoustic Disturbances in a Swirling Mean Flow

We test the nonreflecting boundary conditions for a variety of swirling flows. The propagation of an acoustic disturbance is computed and compared with its eigenvalue solution. As in the uniform flow case, no reflected disturbances should occur and we examine this by computing the transmission coefficients at the downstream boundary. In the ideal case, the transmission coefficient of the incident acoustic wave is one at the downstream boundary and the reflection coefficients are zero. The inflow specification is given for several different mean flows for the parameters shown in table 2. At the inflow boundary, an incident acoustic disturbance with pressure field of the form,

Parameters	Case I	Case II	Case III	Case IV	Case V
$\omega r_m / c_m$	24.18	24.18	24.18	24.18	24.18
m	-12	-12	-12	-12	-12
M_x	.5	.5	.5	.5	.5
r_h / r_t	.65	.65	.65	.65	.65
M_{xm}	.5	.5	.5	.5	.5
$M_{\theta m}$	.4	.4	.4	.4	.4

Table 2: Selected parameters for computing the propagation of sound in a swirling mean flow.

$$\hat{p} = \hat{p}^I = p^+_{mn}(r) e^{i(m\theta + k^+_x x_0)} \tag{64}$$

is imposed. In Figures (16-18), we present the converged numerical solution for the propagation of an acoustic disturbance in a mean flow with free vortex swirl. The grid used is 80 × 25 × 21 in the $x - \theta - r$ directions, respectively. Figure (16) shows the relative error of the calculation versus time iteration and indicates that the converged numerical solution lies within half a percent of the exact solution. In Figures (17-18) the numerical solution is indicated by the solid line, while the exact solution is denoted by the dotted line. Figure (17) shows the solution as a function of axial distance at the intersection of the mid-passage and mid-radius planes. Figure (18) shows the solution variation from hub to tip. Note that the incident disturbance corresponds to the first radial mode since the radial variation of the solution does not cross the axis corresponding to zero pressure from hub to tip. The agreement between the numerical and exact solution is good as the solid lines and dotted lines lie on top of one another. Moreover, the agreement remains good even as we approach the downstream boundary. In order to obtain a quantitative measure, we compute the transmission coefficients at the outflow boundary for the amplitudes of the two largest modes, $a_{-12,1}$ and $a_{-12,2}$. We find the incident mode, $a_{-12,1}$, has an amplitude $a_{-12,1} = .999$. This indicates very little reflection at the downstream boundary. We also find that $a_{-12,2} = .003$, suggesting that the small error in the numerical solution results in weak scattering of the incident mode into another mode.

In Figures (19-21), we present the converged numerical solution for the propagation of an acoustic disturbance in a mean flow with rigid body swirl. In this case, the mean flow is not potential as in the case of free vortex swirl. Figure (19) shows the relative error of the calculation versus time iteration. The numerical solution converges to within half a percent of the exact solution given by the normal mode analysis. The numerical solution is denoted by the solid line while the exact solution denoted by the dotted line. Figure (20) shows the axial variation of the acoustic wave and Figure (21) gives the radial variation of the acoustic wave. The agreement shows that the numerical scheme converges to the correct solution. The outflow boundary transmission coefficient boundary is $a_{-12,1} = .999$ indicating very minor reflection at the downstream boundary. Again weak scattering into the second radial mode occurs at the boundary.

Figure (22) shows the axial variation of the converged numerical solution for a case with mean swirl that is a combination of free vortex and rigid body swirl. The input disturbances was the second radial acoustic mode which crosses the zero pressure axis one time. Again the agreement between the numerical solution and the exact solution is good. Computing the transmission at the outflow boundary, we find $a_{-12,2} = .997$.

The results presented for the acoustic propagation show that the boundary conditions and the numerical interior domain solver converge to the physical solution. These results are further verified by the transmission coefficients for the various mean flow distributions considered. In the next section, we test the boundary conditions on vortical excitations in swirling flow. We also examine the effect that different inflow modeling has on the wake evolution and hence on the aerodynamic response for wake blade/row interaction.

3.5.3 Vortical Disturbances in a Nonuniform Mean Flow

In this section, we prescibe vortical disturbances at the inlet and examine the sensitivity of the wake evolution to the prescribed inlet conditions. A mean flow distribution representative of an engine design is shown in Figure (23). The solution indicates that downstream of the fan, the mean flow contains radial variations in both swirl and axial velocity. The hub-tip ratio for the case is .58. A disturbance was imposed at the inlet with a reduced frequency corresponding to two times blade passing frequency, $\omega = 43$.

We consider inlet excitations where u_x, u_θ are the same, $u_r = 0$ and we examine the effect that different pressure distributions have on the evolution of the vortically-dominated wave. The radial pressure distribution takes the form,

$$p = p_m \sin[\pi i \frac{(r - r_h)}{(r_t - r_h)}], \tag{65}$$

where $p_m = (+.5, 0, -.5)$. The solid line corresponds to p_m positive, the dashed line corresponds to p_m zero and the dot-dashed line corresponds to p_m negative. Note that the case $p_m = 0, u_r = 0$ represents the 'pure convection' approximation which does not satify the Euler equations for nonuniform flows. In Figures (24-27), we plot the axial evolution of the magnitudes of the pressure and velocity field respectively. We see that the pressure magnitude drops very quickly to a small value and does not differ greatly from the zero pressure case. The axial and swirl velocities show differences on the order of $20 - 30$ percent in their magnitude as they evolve downstream. The large drop in pressure near the exit to a small value is consistent with the high frequency analysis which showed that the pressure field associated with the vortically-dominated disturbances is small relative to their velocity field. These results suggest that the evolution of the upwash component of the velocity is only moderately sensitive to the inlet pressure distribution.

The radial velocity perturbation is not negligible upstream of an exit guide vane. However, this information is often neglected from experimetal measurements of the flow field between the fan and the stator. To assess the sensitivity of the upwash evolution with different inlet condition, we consider different radial velocity distributions with u_x, u_θ the same, and $p = 0$. The radial velocity distribution takes the form,

$$u_r = u_{mr} \sin[\pi i \frac{(r - r_h)}{(r_t - r_h)}], \tag{66}$$

where $u_{mr} = (+.5, 0, -.5)$. The solid line corresponds to u_{mr} positive, the dashed line $u_{m\theta}$ zero and the dot-dashed line u_{mr} negative. In Figures (27-28), we plot the evolution of the magnitudes of the pressure and velocity field, respectively, as they propagate downstream. Figure (28), shows that the pressure magnitude drops very quickly to a small value for all three cases. This is expected given the high frequency and circumferential mode order of the case. However, unlike the previous cases, the magnitude of the pressure is markedly different depending on the radial velocity distribution. The radial, swirl and axial velocity components are order one and they show differences in magnitude of nearly one hundred percent one-half of a mean radius downstream of the inlet. This shows that the solution evolution is very sensitive to the prescribed inlet radial velocity distribution.

3.6 Conclusion

Inflow and outflow conditions were formulated and implemented for nonuniform mean flows. It was observed that the numerical solutions were sensitive to the boundary conditions and the details of the inflow excitation. For problems with acoustic waves, the boundary conditions require accurate solutions for the normal modes in a duct. For vortical excitations, the inflow disturbance must be accurately and completely represented. All three components of the wake harmonics must be determined in order to accurately compute the wake upwash component and thus the gust response.

4 Computing the Intensity of Sound in Nonuniform Flow

4.1 Introduction

Often one wishes to determine via experiment or computation the spectral composition and intensity of sound propagating in a duct [23]. In order to determine the intensity of sound, we must separate from the total unsteady field the acoustically-dominated field and determine the energy flux of the acoustic waves. In section 2, we used normal mode analysis to represent the unsteady disturbances in a duct and in section 3 we applied the normal mode analysis to separate the vortically-dominated field from the acoustic disturbances. In this section, we derive an energy relation for acoustic waves propagating in a nonuniform mean flow and we use the normal mode solutions to compute the sound power.

For small-amplitude disturbances to an isentropic irrotational flow an acoustic energy equation can be derived from the Euler equations which depends only on first order quantities [24, 25]. The intensity flux which results is conserved. Myers [26], derived the acoustic energy relation directly from the general energy equation and showed that the acoustic energy represents, to leading order, the energy carried by the unsteady disturbances. In the general case of a nonuniform mean flow, the time-averaged intensity flux is not conserved.

In order to study nonuniform mean flow effects on the propagation of sound energy, we start from the acoustic energy equation for small-amplitude disturbances and derive, in section 4.2, a simplified relation valid in the high frequency limit relevant to the acoustics of fan engines. We note that the nonuniform mean flow, in addition to changing the aerodynamic interaction mechanism and the acoustic modes, also affects the the expression for the acoustic energy as will be discussed in section 4.2. Moreover, as a result of the nonuniformity of the mean flow the duct radial modes are not orthogonal and therefore interference between the different radial modes will modify the computed sound intensity. In section 4.3, we compute the acoustic power for a homentropic mean flow with free vortex swirl to examine the effect that mean flow swirl has on the propagation of acoustic energy in a duct.

4.2 Sound Power in a Nonuniform Flow

The transport of energy by small-amplitude disturbances is governed by the conservation equation [26]

$$\frac{\partial E}{\partial t} + \nabla \cdot \vec{I} = G, \tag{67}$$

where the energy density, E, the energy flux vector, $\vec{I}$, and source term, G, are defined by,

$$E \equiv \frac{p'\rho'}{2\rho_0} + (\rho_0|u|^2 + \rho'\vec{u}\cdot\vec{U}_0), \quad \vec{I} \equiv (\frac{p'}{\rho_0} + \vec{u}\cdot\vec{U}_0)(\rho_0\vec{u} + \rho'\vec{U}), \tag{68}$$

$$G \equiv \vec{u}\cdot[\vec{U}_0 \times (\rho_0 \vec{\zeta}' - \vec{\zeta}_0 \rho')] + \frac{(\vec{u} + \frac{\rho'}{\rho_0}\vec{U}_0)}{\rho_0}\cdot(\rho'\nabla p_0 - p'\nabla\rho_0) + \frac{1}{2\rho_0}(\rho'\frac{\partial p'}{\partial t} - p'\frac{\partial \rho'}{\partial t}) \quad (69)$$

From equation (12), the mean radial velocity is zero and the term, $\frac{\rho'}{\rho_0}\vec{U}_0\cdot(\rho'\nabla p_0 - p'\nabla\rho_0)$ vanishes. Note that the expressions for the energy and energy flux are second order expressions which depend only on first order quantities. As a result, the energy of the unsteady disturbances can be computed as a by-product of the linearized Euler equations. Expressing the last four terms in G in terms of the entropy, equation (67) becomes

$$\frac{\partial E}{\partial t} + \nabla\cdot\vec{I} = \vec{u}\cdot[\vec{U}_0 \times (\rho_0\vec{\zeta}' - \vec{\zeta}_0\rho') + \frac{1}{c_p}(p'\nabla S_0 - s'\nabla p_0)] + \frac{c_0^2}{2c_p}(\rho'\frac{\partial s'}{\partial t} - s'\frac{\partial \rho'}{\partial t}). \quad (70)$$

Equation (70) shows that the disturbance field interacts with the mean flow and mean flow gradients to transfer energy between the mean flow and the propagating disturbances.

4.2.1 Acoustic Energy in the High Frequency Limit

In fan engine aeroacoustic calculations, the frequencies of the noise source are often high. For example, in tone noise the frequency is $(nB\Omega)$ where n is the harmonic index, B is the number of blades and Ω is the shaft rotation frequency. As a result, the characteristic acoustic wavelength is $\ell = c_m/(nB\Omega) = r_m/(nBM_m)$ where M_m is the rotational Mach number at the mean radius of the fan. However, variations in the mean flow are characterized by the mean radius of the duct. In the high frequency limit, $\ell/r_m << 1$. In this limit, the vorticity content of the acoustic waves is small [14]. To examine the relative order of the various terms in (70), we introduce the fast variables,

$$\begin{aligned} \tilde{\vec{x}} &= \vec{x}/\epsilon, \\ \tilde{t} &= t/\epsilon, \end{aligned} \quad (71)$$

where $\epsilon = \ell/r_m << 1$. Substituting into (9) we obtain,

$$\frac{D_0}{D\tilde{t}}s' + \epsilon(\vec{u}\cdot\nabla)S_0 = 0, \quad (72)$$

where $\frac{D_0}{D\tilde{t}} \equiv \frac{\partial}{\partial \tilde{t}} + \vec{U}_0\cdot\tilde{\nabla}$ and $\tilde{\nabla} = \epsilon\nabla$. Equation (72) shows that to leading order the unsteady entropy field is convected with the mean flow,

$$\frac{D_0}{D\tilde{t}}s' = 0, \quad (73)$$

over the small distance, ℓ.

Substituting (71) into (70), we obtain to leading order

$$\frac{\partial E}{\partial \tilde{t}} + \tilde{\nabla} \cdot \vec{I} = \vec{u} \cdot [\rho_0(\vec{U}_0 \times \vec{\tilde{\zeta}}')] + \frac{c_0^2}{2c_p}(\rho' \frac{\partial s'}{\partial \tilde{t}} - s' \frac{\partial \rho'}{\partial \tilde{t}}). \tag{74}$$

Note that $\vec{\tilde{\zeta}}' = \epsilon \vec{\zeta}'$ is $O(|\vec{u}|)$. Equation (74) shows that the acoustic intensity is no longer a conserved quantity as a consequence of the unsteady entropy and the interaction between the unsteady vorticity and the mean flow. When incident waves are only acoustic, then $\vec{\zeta}'$ is small [14] and from (72) s' is $O(\epsilon \vec{u}|)$. As a result, the acoustic intensity is locally conserved over a distance ,$O(\ell)$, which is small relative to the mean radius. In the general case, the disturbance field contains both acoustic and vortical parts. However, in the high frequency limit, the two parts can be decoupled since, as was shown in section 3, the pressure field associated with the nearly-convected modes is small. Thus, taking only acoustic part of the disturbance field and substituting into (74) we find that the acoustic energy is locally conserved, *i. e.*

$$[\frac{\partial E}{\partial \tilde{t}} + \tilde{\nabla} \cdot \vec{I}]_A = 0, \tag{75}$$

where the subscript A denotes the acoustic part of the unsteady field.

4.3 The Sound Power in a Homentropic Mean Flow

In this section, we use the normal mode analysis to define acoustic disturbances in a homentropic flow. We then derive the sound power and examine the contributions of various terms in the sound power for a case of free vortex swirling flow. When calculating the sound energy in an annular duct, we are mainly interested in the mean flux of acoustic energy across an axial plane. The axial component of the intensity then reduces to

$$I_x = (p'/\rho_0 + M_x u_x + M_s u_\theta)(\rho_0 u_x + M_x p'). \tag{76}$$

Note the expression for the axial intensity has two terms which contain the swirl velocity. Substituting (17) into the momentum equations we obtain expressions for the modal velocity field in terms of the pressure and radial velocity,

$$u_{mn_r} \quad = \quad a_{mn} f_{mn}(r) e^{i(k_{mn}x + m\theta)}$$

$$
\begin{aligned}
u_{mn_x} &= a_{mn}\frac{(i\frac{d}{dr}M_x f_{mn} - k_{mn}p_{mn}/\rho_0)}{\Lambda_{mn}}e^{i(k_{mn}x+m\theta)} \\
u_{mn_\theta} &= a_{mn}\frac{[i\frac{1}{r}\frac{d}{dr}(rM_s)f_{mn} - (mp_{mn})/(r\rho_0)]}{\Lambda_{mn}}e^{i(k_{mn}x+m\theta)}
\end{aligned}
\tag{77}
$$

where

$$
f_{mn} = -i\frac{(\frac{2mM_s p_{mn}}{r^2\rho_0} + \Lambda_{mn}\frac{d}{dr}(p_{mn}/\rho_0))}{(\frac{2M_s}{r^2}\frac{d}{dr}(rM_s) - \Lambda_{mn}^2)}. \tag{78}
$$

Substituting (77) into (76) and integrating across an axial surface we obtain the sound power in the duct,

$$
\begin{aligned}
\Pi &= \pi\Re\Big\{\sum_{n=1}^{n=N_r}\sum_{n'=1}^{n=N_r}\sum_{m=1}^{m=N_\theta} a_{mn}a_{mn'}^{*}e^{i(k_{mn}-k_{mn'})x}\int_{r_h/r_m}^{r_t/r_m} r[(1+\frac{M_x^2}{c_0^2})p_{mn}u_{mn'_x}^{*} \\
&+\frac{M_x}{\rho_0 c_0^2}p_{mn}p_{mn'}^{*} + \frac{M_xM_s}{c_0^2}p_{mn}u_{mn'_\theta}^{*} + \rho_0 M_x u_{mn_x}u_{mn'_x}^{*} + \rho_0 M_s u_{mn_x}u_{mn'_\theta}^{*}]dr\Big\},
\end{aligned}
\tag{79}
$$

where N_r and N_θ are the number of radial and circumferential propagating modes, $*$ is used to denote the complex conjugate and $\Re$ denotes the real part. Since the mean flow is potential and isentropic, the time averaged intensity flux is conserved.

Note that in a swirling mean flow, the eigenfunctions are not orthogonal. As a result, interference occurs between different radial modes. Note that the sound power varies with x for the interference modes $n \neq n'$. Thus, the conservation of sound power requires that the sum of the modal powers corresponding to the interference modes must be zero, *i. e.*,

$$
\begin{aligned}
&\sum_{n=1}^{n=N_r}\sum_{n'=1}^{n=N_r}\int_{r_h/r_m}^{r_t/r_m} r[(1+\frac{M_x^2}{c_0^2})p_{mn}u_{mn'_x}^{*} + \frac{M_x}{\rho_0 c_0^2}p_{mn}p_{mn'}^{*} + \frac{M_xM_s}{c_0^2}p_{mn}u_{mn'_\theta}^{*} \\
&+\rho_0 M_x u_{mn_x}u_{mn'_x}^{*} + \rho_0 M_s u_{mn_x}u_{mn'_\theta}^{*}]dr = 0 \quad n \neq n'.
\end{aligned}
\tag{80}
$$

The purpose of the next subsection is to check this result in a homentropic and potential mean flow and to determine which of the terms in (79) are the major contributors to the sound power.

4.3.1 Numerical Results for a Free Vortex Swirling Flow

In a free vortex swirling flow, acoustic disturbances propagating in a duct are purely potential and conserve acoustic energy. To examine the major contributions to the sound power and study the effect of swirl, we compute the contributions to the modal sound power from each of the terms in equation (79). We consider a free vortex swirling flow in an annular duct, as shown in Figure (32). The plot shows that the annulus extends from a non-dimensional radius of .8 to 2.0 and the swirl Mach number is inversely proportional to the radius. To conserve sound power, the sum of the contribution of each interference term inside the integral in equation (80) must be zero so that there is no x-dependence in the sound power. Thus, although the eigenfunctions are not orthogonal, the contribution of interference terms to the sound power should be negligible.

In Figure (33), we show the contributions of each of the terms in the integral for the downstream propagating modes corresponding to a case with reduced frequency, $\omega = 20$ and spinning mode order, $m = -1$. The open circle, + and $*$ correspond to the contributions of the first three terms in (80), respectively and the x and diamond correspond to the fourth and fifth terms. The abscissa corresponds to the radial mode index n' and the ordinate represents the contribution of each term. The different figures correspond to different radial mode orders, n for a given spinning mode order, m. The index, n, describes the eigenfunction which has $n-1$ zero crossings from the hub to tip. In this case, there exist 6 propagating modes. The contribution of the interference terms are quite small relative to the noninterference terms, $n = n'$. Also the dominant contributions to the power result from the contributions of the first, second and fourth terms. For the highest order radial mode, $n = 6$, the first two terms contribute the most to modal power. As the mode order decreases, the contribution of the first term increases rapidly from a value of .25 to nearly one. The second term does not change appreciably for the various mode orders but the contribution of the fourth term becomes significant for the lower order radial modes. For this case, with low spinning mode order, $m = -1$, the third and fifth terms which contain the swirl component of the mean velocity produce negligible contributions to the modal power. Summing the noninterference terms of the six modes we find the contribution is of the order 1×10^{-3} as opposed to the noninterference terms which result in $O(1)$ contributions to the power.

In Figure (34), we consider a case with a reduced frequency of 50 and spinning mode order $m = -16$. In this case, there exist 15 propagating modes which are again ordered based on the number of zero crossings that occur between the hub and the tip. We consider the six upstream propagating modes which range from $n = 9$ to $n = 14$. Again the first, second and fourth terms contribute the most to the sound power. As in the previous case, the contribution of the fourth term increases for the lower radial modes. Interference between the different radial modes was observed but the magnitude of the interference terms were $O(10^{-2})$ as opposed to the noninterference contributions which are $O(1)$. The most significant interference contributions occurred from the modes adjacent to the $n = n'$ mode.

Finally, we consider a case with reduced frequency, 24.5 and spinning mode order $m = -28$. In Figure (35), we show the modal power contributions for each term in (79) . In this case, the swirl plays a more significant role in the modal power. The third term in (79) is most significant for the higher order radial modes. Contributions from the interference terms are evident in this case. However, their summed contributions remain small, *i. e.* $O(10^{-3})$.

4.4 Conclusions

An expression for the sound power was derived which is valid for nonuniform flows. For high frequency disturbances, the propagation of sound energy can be treated as locally conserved. The dominant contributions to the sound power were computed for several unsteady acoustic disturbances. These results can be used in conjunction with an aeroacoustic calculation to compute the sound power and determine the major modal contributors to noise. For the case of a free vortex mean flow swirl, interference effects were negligible. However, these results must be examined for more general nonuniform mean flows.

Acknowledgements The author would like to thank Professor H. M. Atassi and his students, Amr Ali and Basman Hadidi for their help and collaboration on this project. Much of this work builds upon and uses the work they have done in this area over the last several years. The author would also like to thank Dr. Wesley Lord for his suggestion to generalize this work to mean flows with arbitrary radial distributions. Finally, the author would like to thank Dennis Huff as contract monitor for his steadfast support of this work.

References

[1] Giles, M. B. Nonreflecting Boundary Conditions for Euler Equation Calculations. *AIAA Journal*, 28:250–258, 1990.

[2] Fang, J. and Atassi, H. M. Aerodynamics of Loaded Cascades in Subsonic Flow Subject to Unsteady Three-Dimensional Vortical Disturbances. *AIAA Paper 92-0146*

[3] O. V. Atassi. Inflow/outflow conditions for time-harmonic internal aeroacoustic problems. In *AIAA 99-0482, 37th AIAA aerospace sciences meeting and exhibit, Jan. 11-14, Reno, NV*, 1999.

[4] Montgomery, M. D. and Verdon, J. M. A Three-Dimensional Linearized Unsteady Euler Analysis for Turbomachinery Blade Rows. *NASA CR-4770, 1997*

[5] Atassi, H. M. Unsteady Aerodynamics of Vortical Flows: Early and Recent Developments, in K.-Y. Fung (ed.), *Aerodynamics and Aeroacoustics*, World Scientific, pp. 121-172.

[6] Kerrebrock, J. L. Small Disturbances in Turbomachine Annuli with Swirl. *AIAA Journal*, 15:794–803, 1977.

[7] Golubev, V. V. and Atassi, H. M. Acoustic-Vorticity Waves in Swirling Flows *Journal of Sound & Vibration*, 209:203–222, 1998.

[8] V. V. Golubev and H. M. Atassi. Unsteady swirling flows in annular cascades. part I: evolution of incident disturbances. *AIAA Journal*, 38:1142-1149, 2000.

[9] M. Namba. Three-dimensional flow, 1987. In Unsteady Turbomachinery Aerodynamics, AGARD-AG-298.

[10] Donald Hanson. Theory for broadband noise of rotor and stator cascades with inhomogenuous inflow turbulence- including effects of lean and sweep, 1999. NASA CR-27727.

[11] Stewart Glegg and Natasha Walker. Fan noise from blades moving through boundary layer turbulence. In *Fifth AIAA/CEAS Aeroacoustics Conference*, 1999.

[12] J. M. Tayler and T. G. Sofrin. Axial flow compressor noise studies. *SAE Transactions*, 70:309–332, 1962.

[13] V. V. Golubev and H. M. Atassi. Sound propagation in an annular duct with mean potential swirling flow. *Journal of Sound and Vibration*, 198(5):601–616, 1996.

[14] V. V. Golubev and H. M. Atassi. Acoustic-vorticity waves in swirling flows. *Journal of Sound and Vibration*, 209(2):203–222, 1998.

[15] K. A. Kousen. Eigenmode analysis of ducted flows with radially dependent axial and swirl components. In *First Joint CEAS/AIAA Aeroacoustics Conference*, pages 1085–1104, 1995.

[16] A. A. Ali, O. V. Atassi and H. M. Atassi. Acoustic eigenmodes in an annular duct with a general swirling flow. In *6th AIAA/CEAS Aeroacoustics Conference at Maui,Hawaii*

[17] O. V. Atassi and W. Lord. Private communication.

[18] H. C. Ku and D. Hatziavramidis. Chebyshev expansion methods for the solution of the extended graetz problem. *Journal of Computational Physics*, 56:495–512, 1984.

[19] W. H. Press, S. A. Teukolsky, W. T. Vetterling, and B. P. Flannery. *Numerical Recipes in FORTRAN: The art of Scientific Computing.* Cambridge University Press, 1988.

[20] V. V. Golubev and H. M. Atassi. Unsteady swirling flows in annular cascades. part II. Aerodynamic Blade Response. *AIAA Journal*, 38:1151-1158, 2000.

[21] Elhadidi, B. M. and Atassi, H. M. and Envia, E. and Podboy, G. *Evolution of Rotor Wake in Swirling Flow.* In *6th AIAA/CEAS Aeroacoustics Conference at Maui,Hawaii.*

[22] Hanson, D. B., "Fan Stator with Harmonic Excitation by Rotor Wake" 3rd CAA Workshop on Benchmark Problems, Category 4, 1999.

[23] Ganz, Ulrich W., Joppa, Paul D., Patten, Timothy & Scharpf, Daniel F. Boeing 18" Fan Rig Broadband Noise Test" *NASA CR 1998-208704*

[24] Blokhintsev, D. I. Acoustics of a Nonhomogenuous Moving Medium *Translated NASA Technical Memorandum, No. 1399., 1956*

[25] Morfey, C. L. Acoustic Energy in Nonuniform Flows *Journal of Sound & Vibration*, 14:159–170, 1971.

[26] Myers, M. K. An Exact Energy Corollary for Homentropic Flow. *Journal of Sound & Vibration*, 109:277–284, 1986.

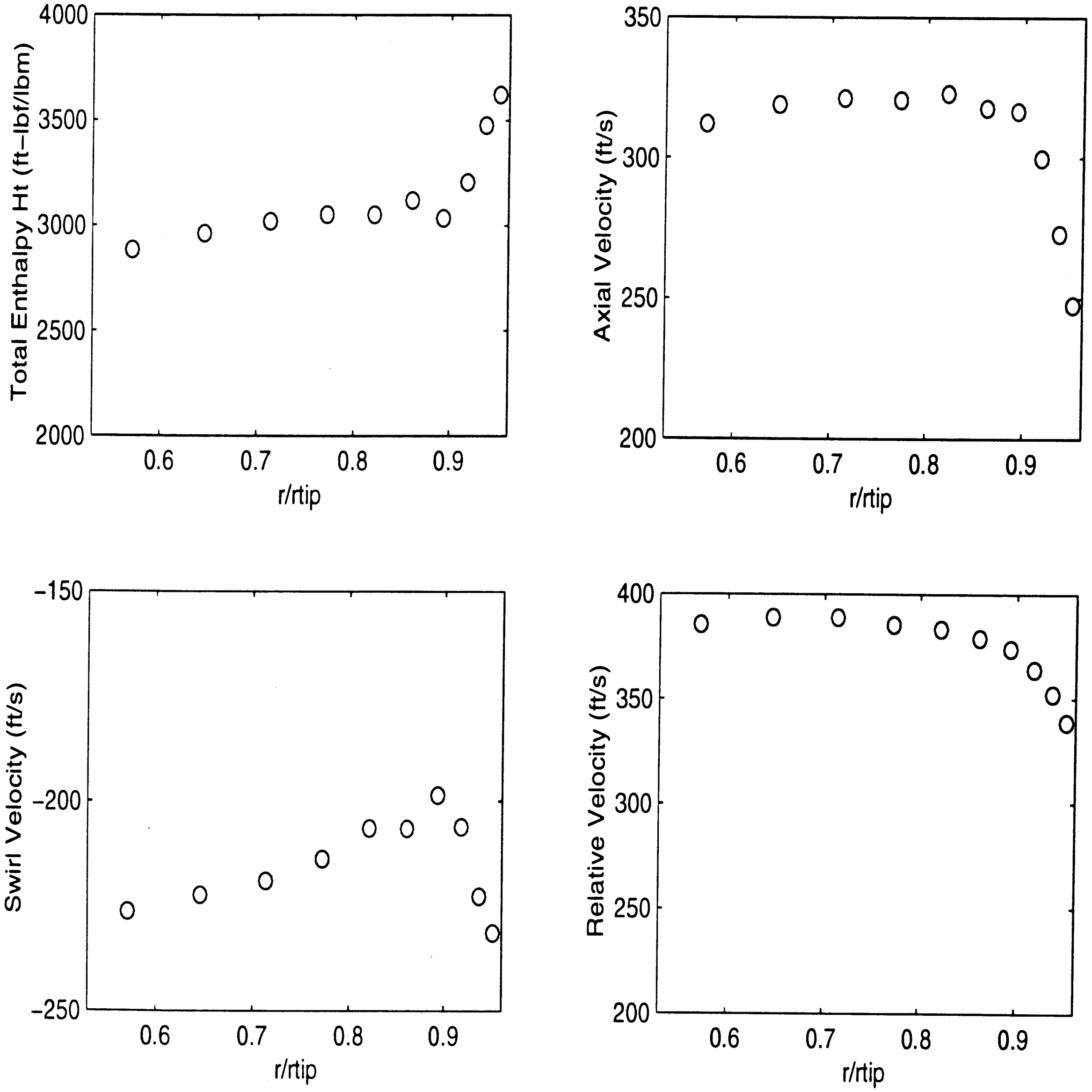

Figure 1: The radial profile of the mean velocity and total enthalpy for a plane lying between a fan and an exit guide vane. The computational results were obtained using a Reynolds averaged Navier Stokes code and show the strongest radial variations in the tip region of the annulus where the tip vortex of the fan lies.

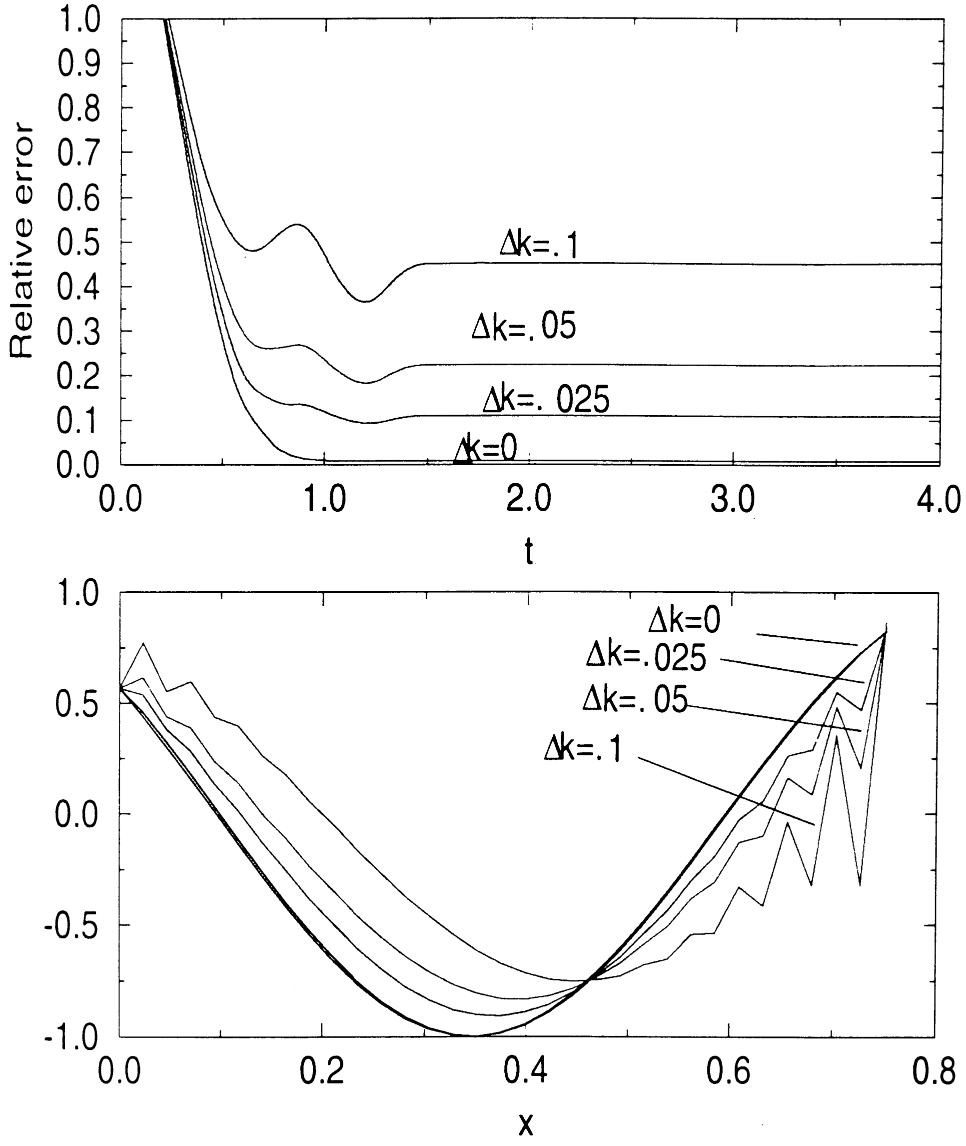

Figure 2: Effect of Error in Nonreflecting Boundary Conditions on Numerical solution. Row 1 shows the global relative error in the numerical solution versus time. Row 2 shows the real part of the numerical solution along the one-dimensional domain for increasing errors in the boundary condition, Δk.

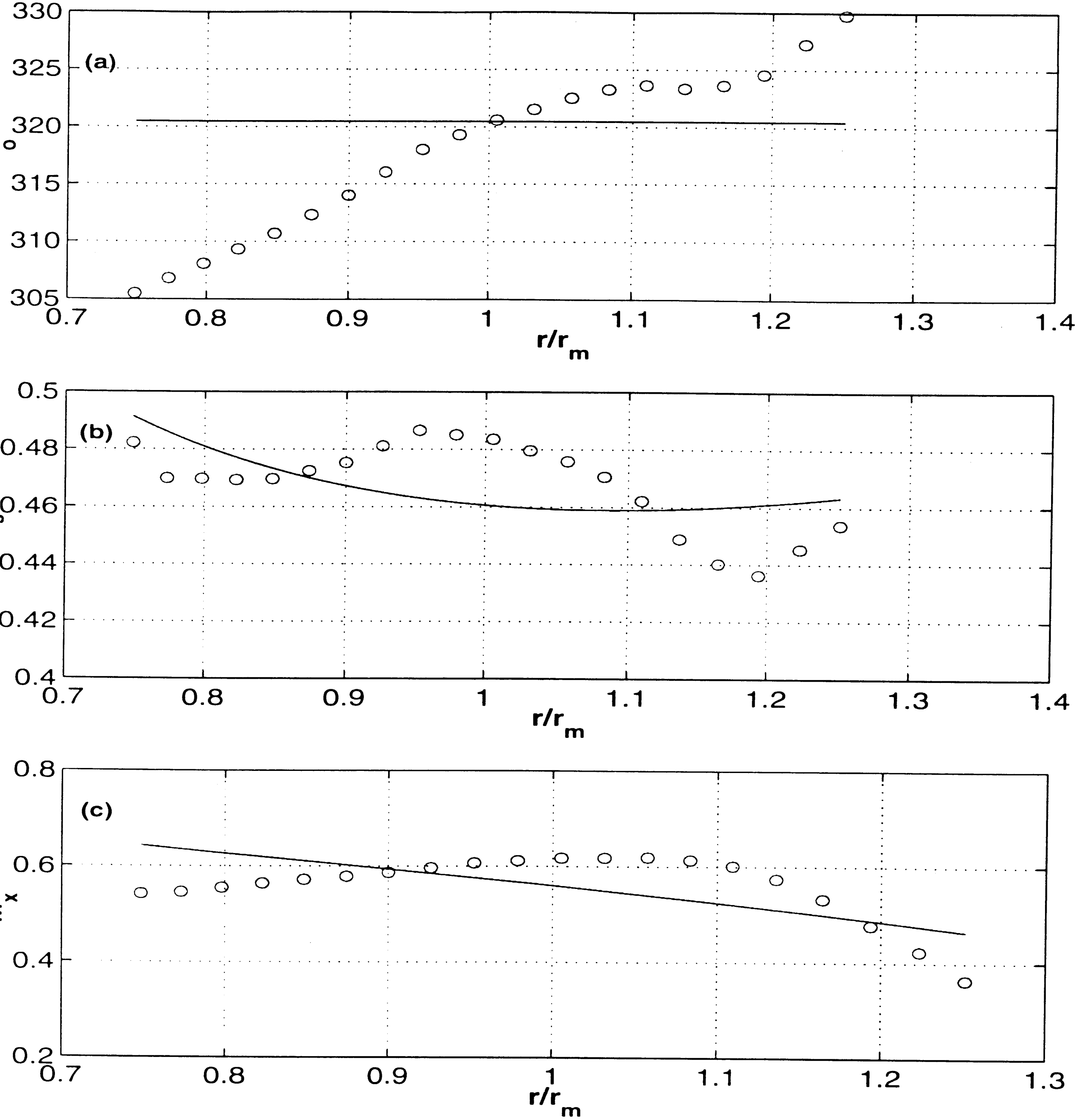

Figure 3: Plots comparing a theorectical mean flow model based on a combination of free vortex and rigid body swirl. The mean flow model is represented by the solid line and the data is represented by the ircles.

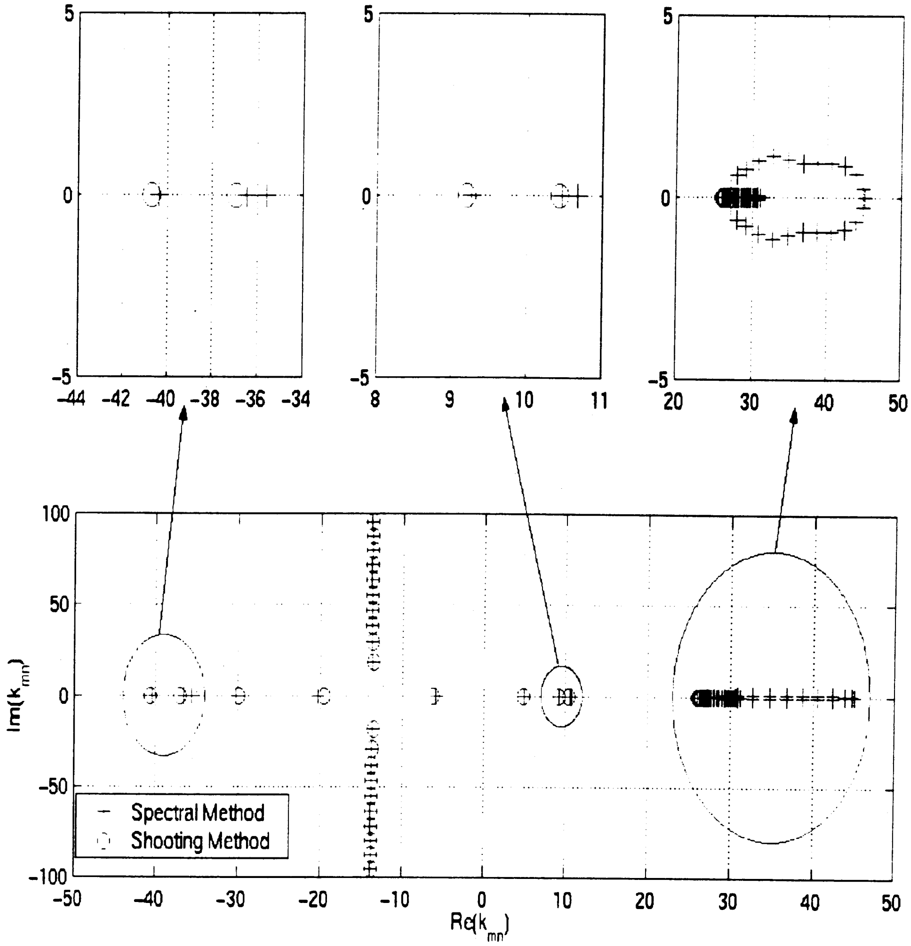

Figure 4: Comparison of eigenmodes spectra obtained using the spectral method and the shooting method, $m = -1$, $\omega = 16$. The plus symbol denotes the initial guess obtained by the spectral method and the open circle denotes the final converged solution which is obtained by the shooting method. Note that the spectral method shows five upstream and downstream propagating modes, while the shooting method indicates that there are only four propagating modes.

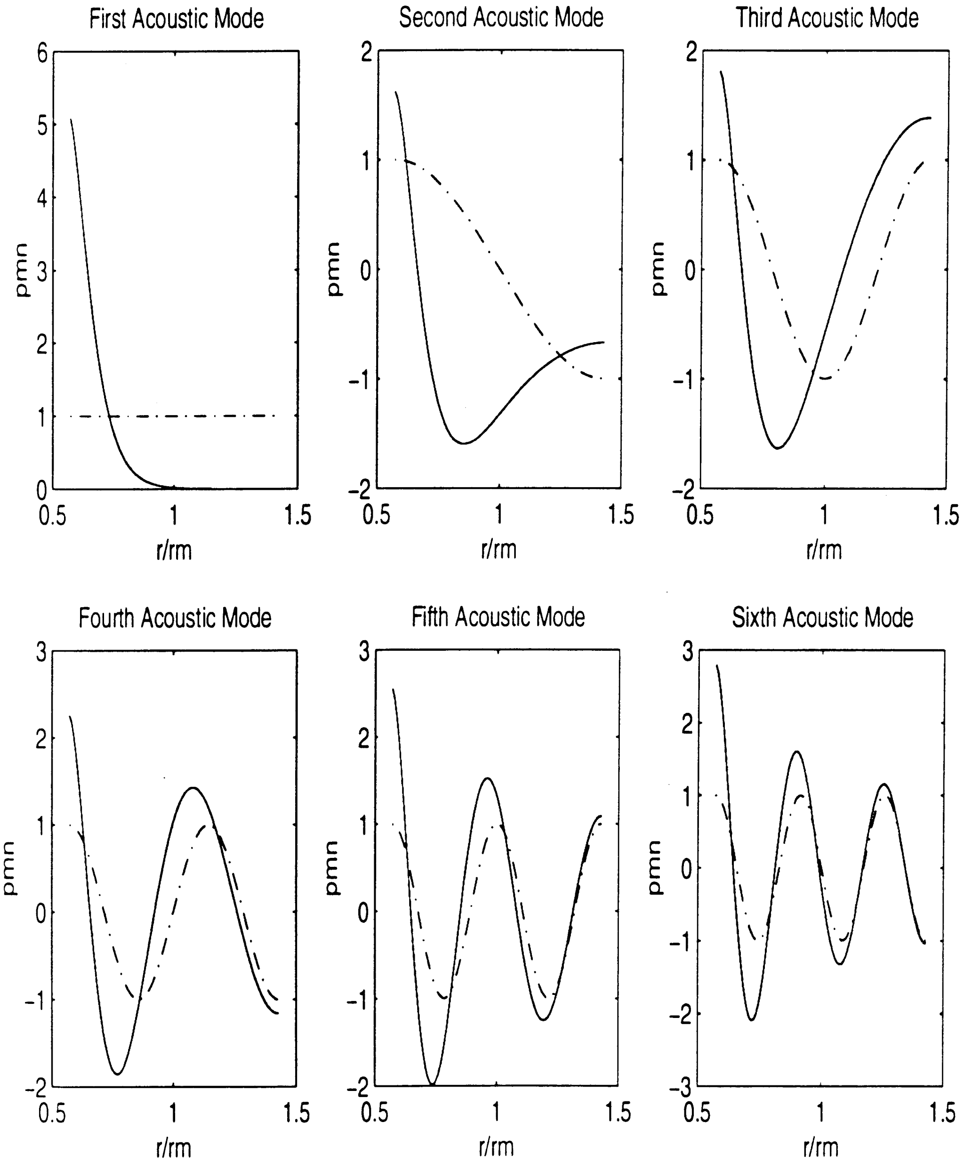

Figure 5: Eigenfunctions of six downtream propagating acoustic modes. $m = -1$, $\omega = 20. \frac{r_h}{r_t} = .4$. The solid line is the analytical solution based on the narrow annulus limit and the dashed line is the numerical solution. Note the large differences in the eigenfunctions near the hub.

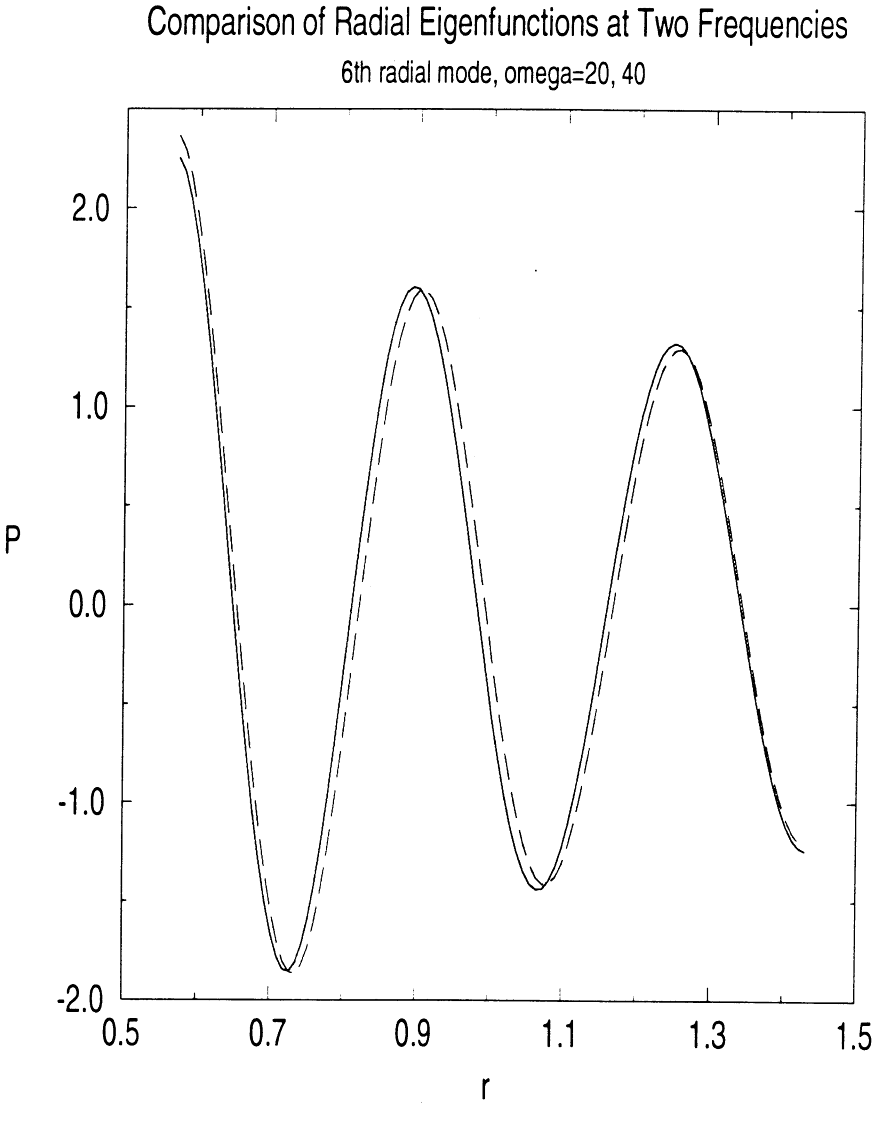

Figure 6: Comparison of the sixth radial mode of downstream propagating acoustic modes , $m = -1$, $\frac{r_h}{r_t} = .4$, at two different frequencies, $\omega = 20, 40$

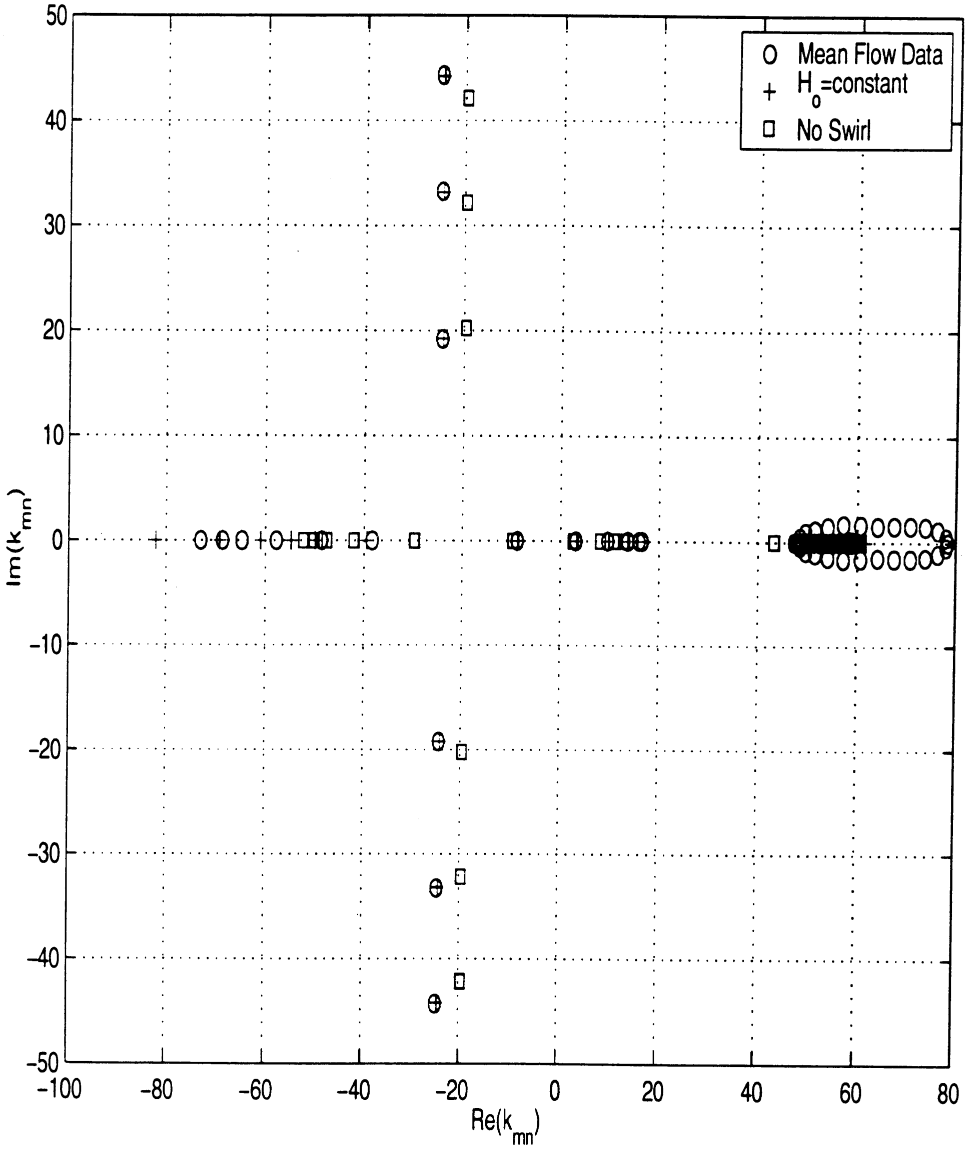

Figure 7: Eigenmode spectra for different mean flow models, $m = -12$, $\omega = 24.2$. Note that the mean flow modifies the upstream propagating modes more than the downstream propagating modes.

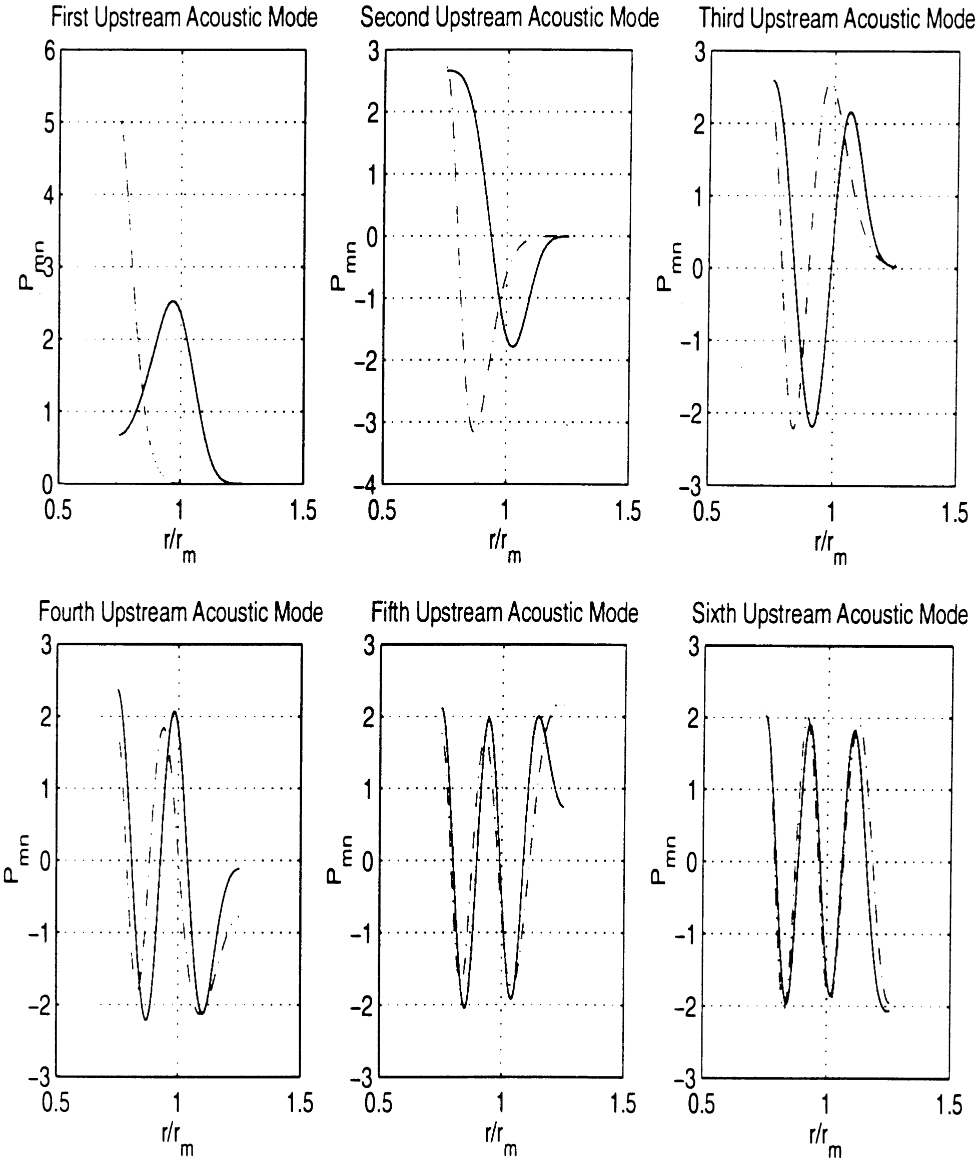

First Upstream Acoustic Mode

Second Upstream Acoustic Mode

Third Upstream Acoustic Mode

Fourth Upstream Acoustic Mode

Fifth Upstream Acoustic Mode

Sixth Upstream Acoustic Mode

Figure 8: Eigenfunctions of upstream propagating acoustic modes, $m = -12$, $\omega = 24.2$; '-' mean flow data, '-.' theoretical mean flow model. Note that the theoretical mean flow model provides an accurate representation of the higher order radial modes but does not do well for the first two radial modes.

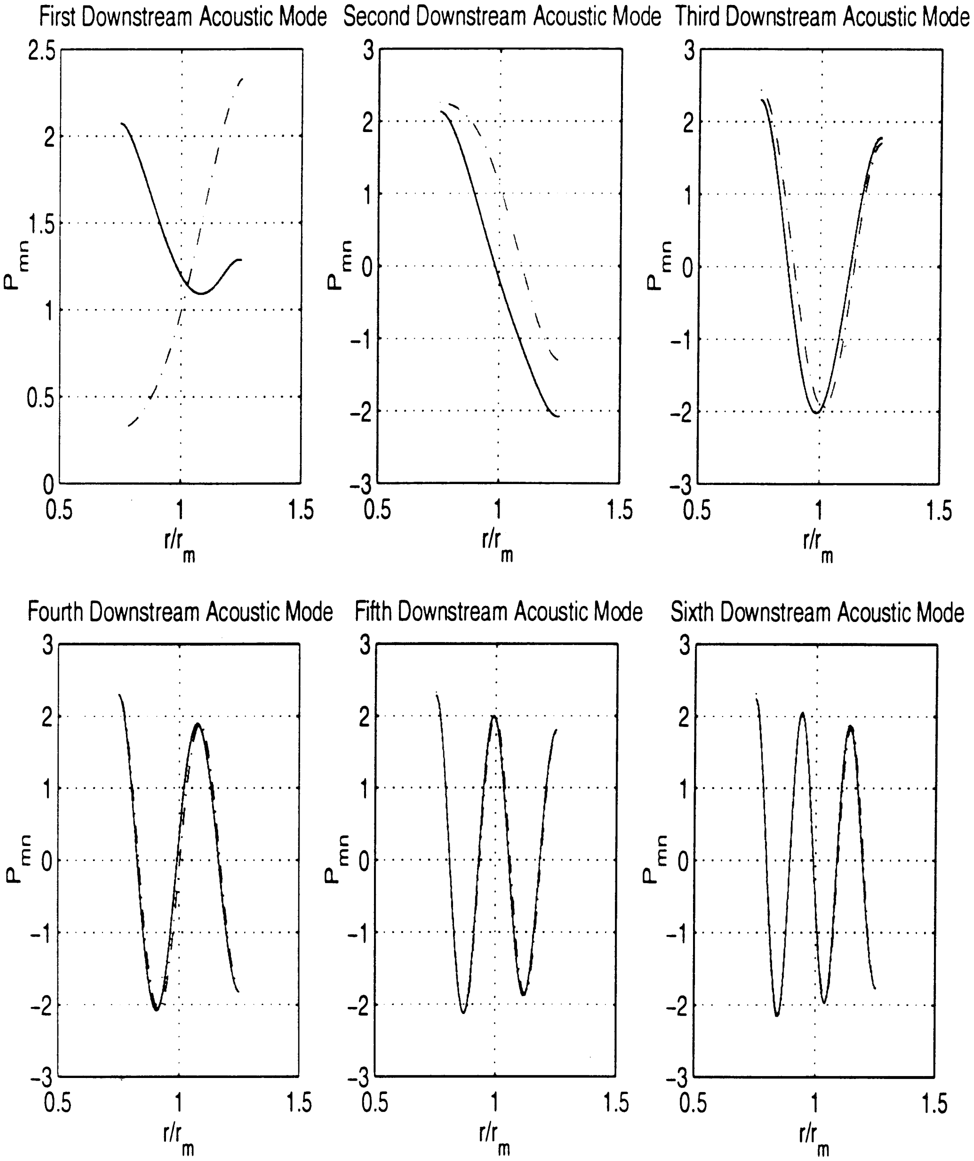

Figure 9: Eigenfunctions of downstream propagating acoustic modes, $m = -12$, $\omega = 24.2$; '-' mean flow data, '-.' theoretical mean flow model. The eigenfunction solution using the theoretical mean flow model provides a good approximation except for the first radial mode.

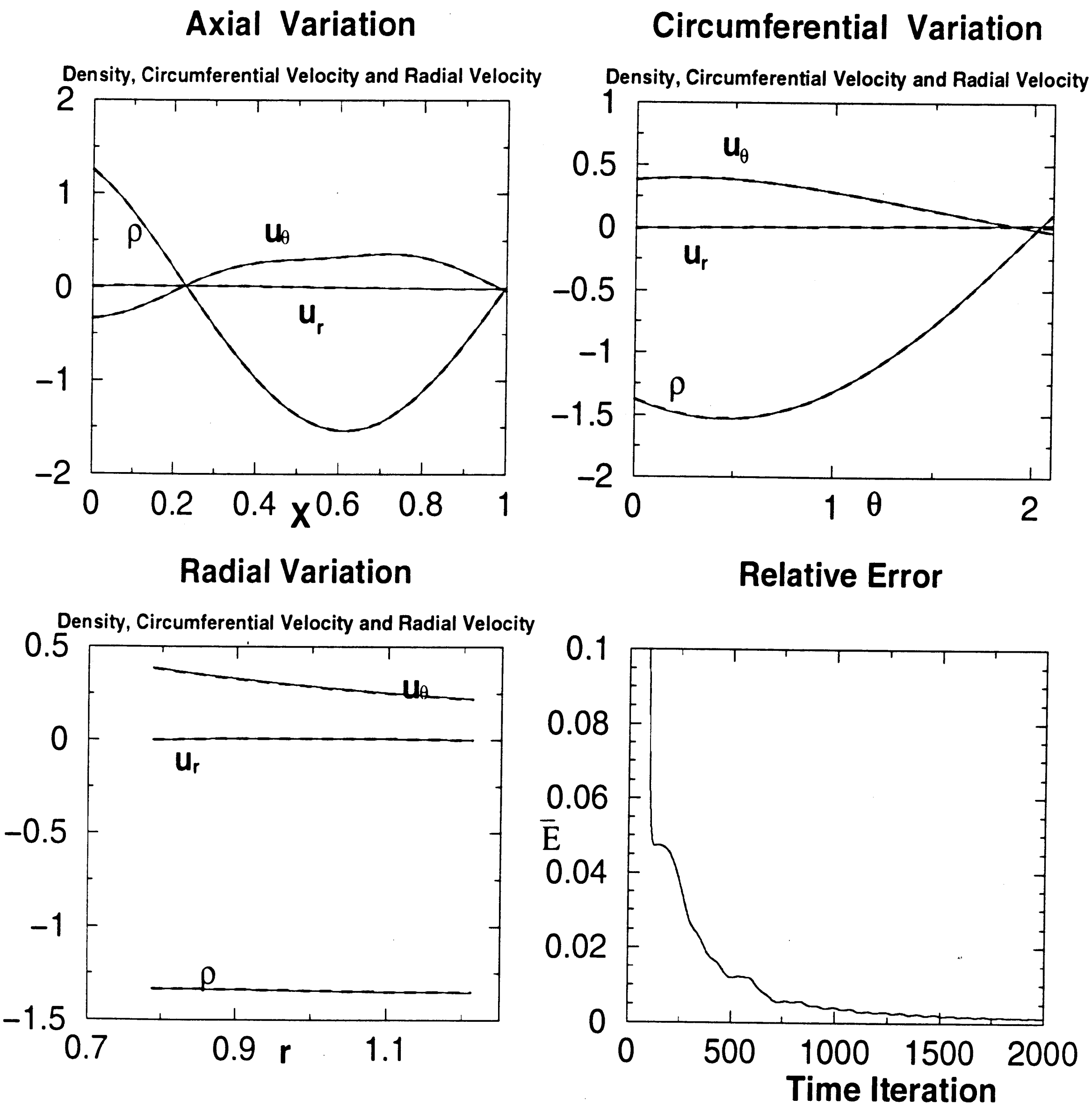

Axial Variation

Circumferential Variation

Radial Variation

Relative Error

Figure 10: A superposition of a vortical and an acoustic disturbance is imposed upstream. The hub-tip ratio is .65 and the radial phase variation is such that a quarter of a wavelength fits between the hub and the tip. The numerical solution of the density and two components of the velocity are plotted as solid lines as a function of x, θ and r at the midplanes of the duct respectively. The exact solution is shown by the dashed lines. The global relative error of the density is plotted in the bottom right figure as a function of time iteration.

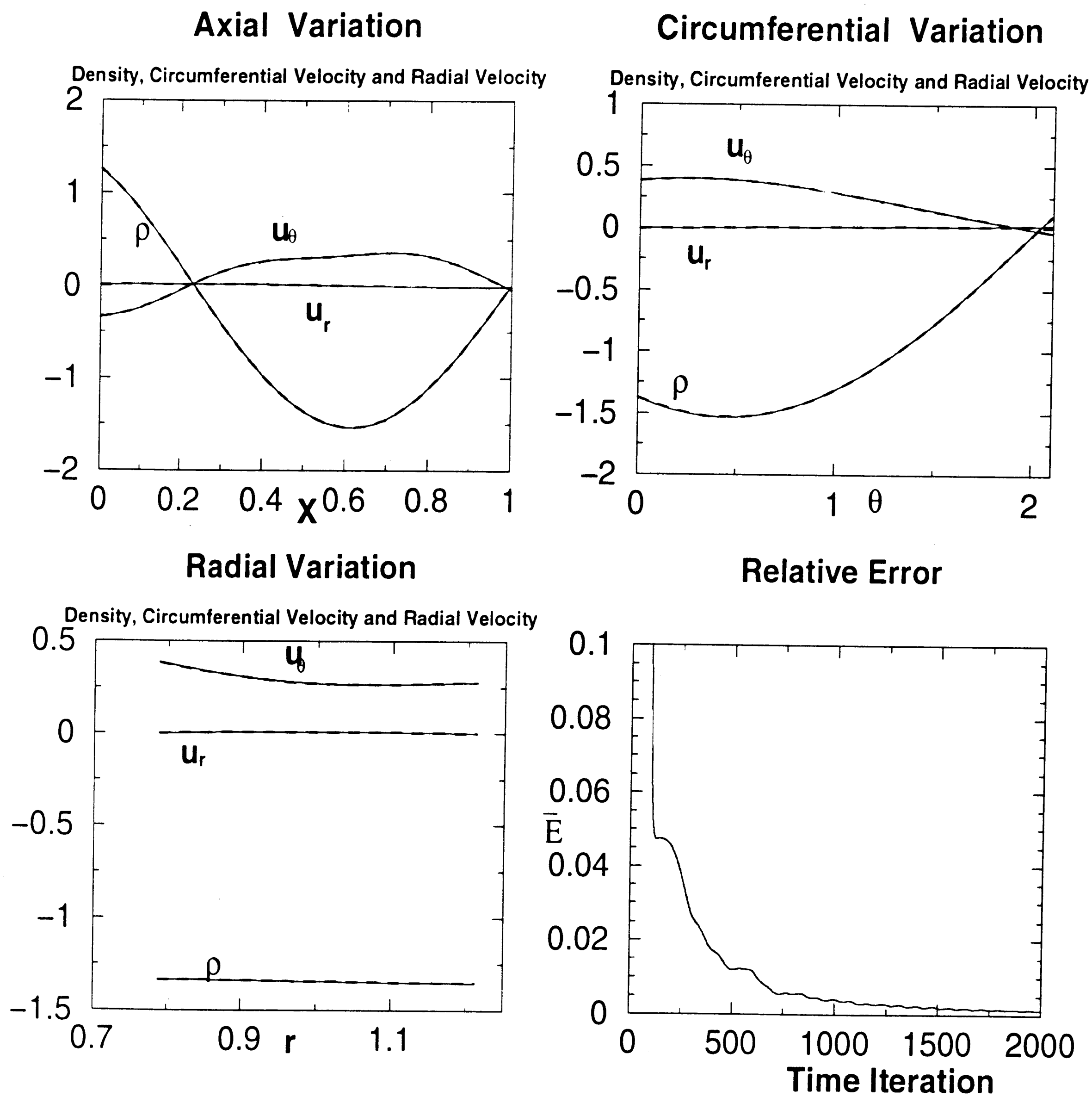

Figure 11: A superposition of a vortical and an acoustic disturbance is imposed upstream. The hub-tip ratio is .65 and the radial phase variation is such that a half of a wavelength fits between the hub and the tip. The numerical solution of the density and two components of the velocity are plotted as solid lines as a function of x, θ and r at the midplanes of the duct respectively. The exact solution is shown by the dashed lines. The global relative error of the density is plotted in the bottom right figure as a function of time iteration.

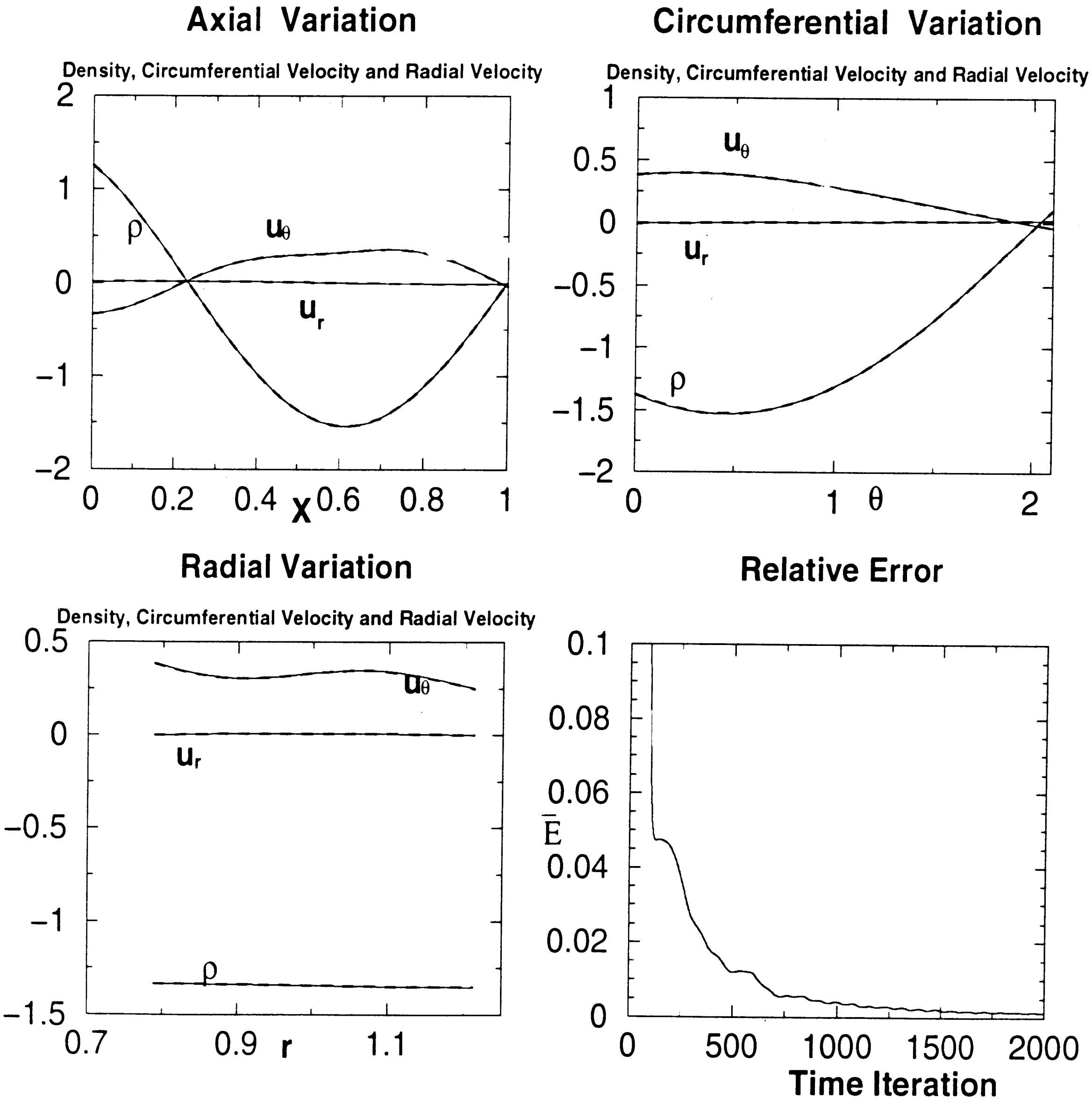

Figure 12: A superposition of a vortical and an acoustic disturbance is imposed upstream. The hub-tip ratio is .65 and the radial phase variation is such that a full wavelength fits between the hub and the tip. The numerical solution of the density and two components of the velocity are plotted as solid lines as a function of x, θ and r at the midplanes of the duct respectively. The exact solution is shown by the dashed lines. The global relative error of the density is plotted in the bottom right figure as a function of time iteration.

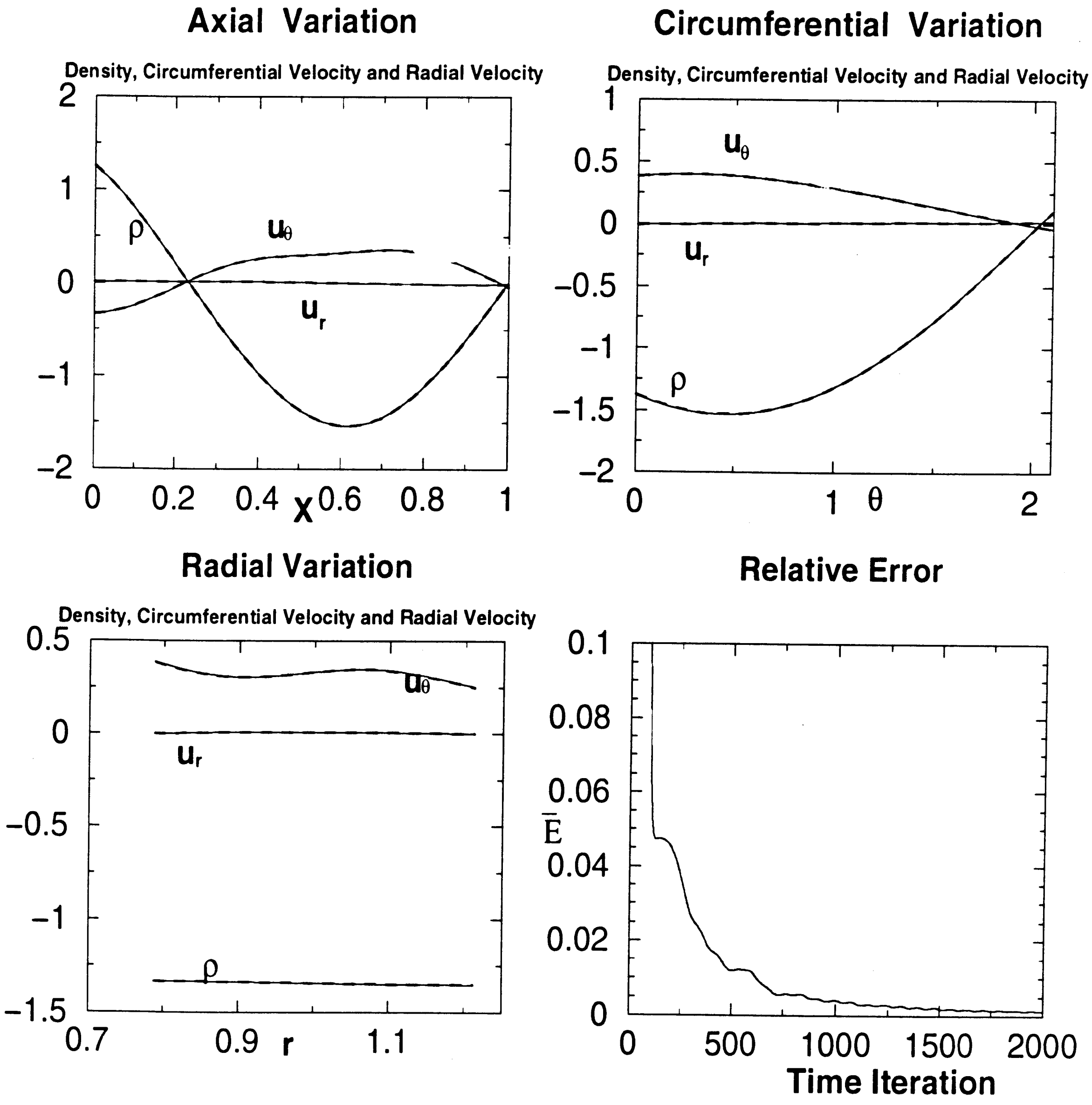

Figure 13: A superposition of a vortical and an acoustic disturbance is imposed upstream. The hub-tip ratio is .65 and the radial phase variation is such that a full wavelength fits between the hub and the tip. The amplitude of the acoustic wave is 1.0 The numerical solution of the density and two components of the velocity are plotted as solid lines as a function of x, θ and r respectively. The exact solution is shown by the dashed lines. The global relative error of the density is plotted in the bottom right figure as a function of time iteration.

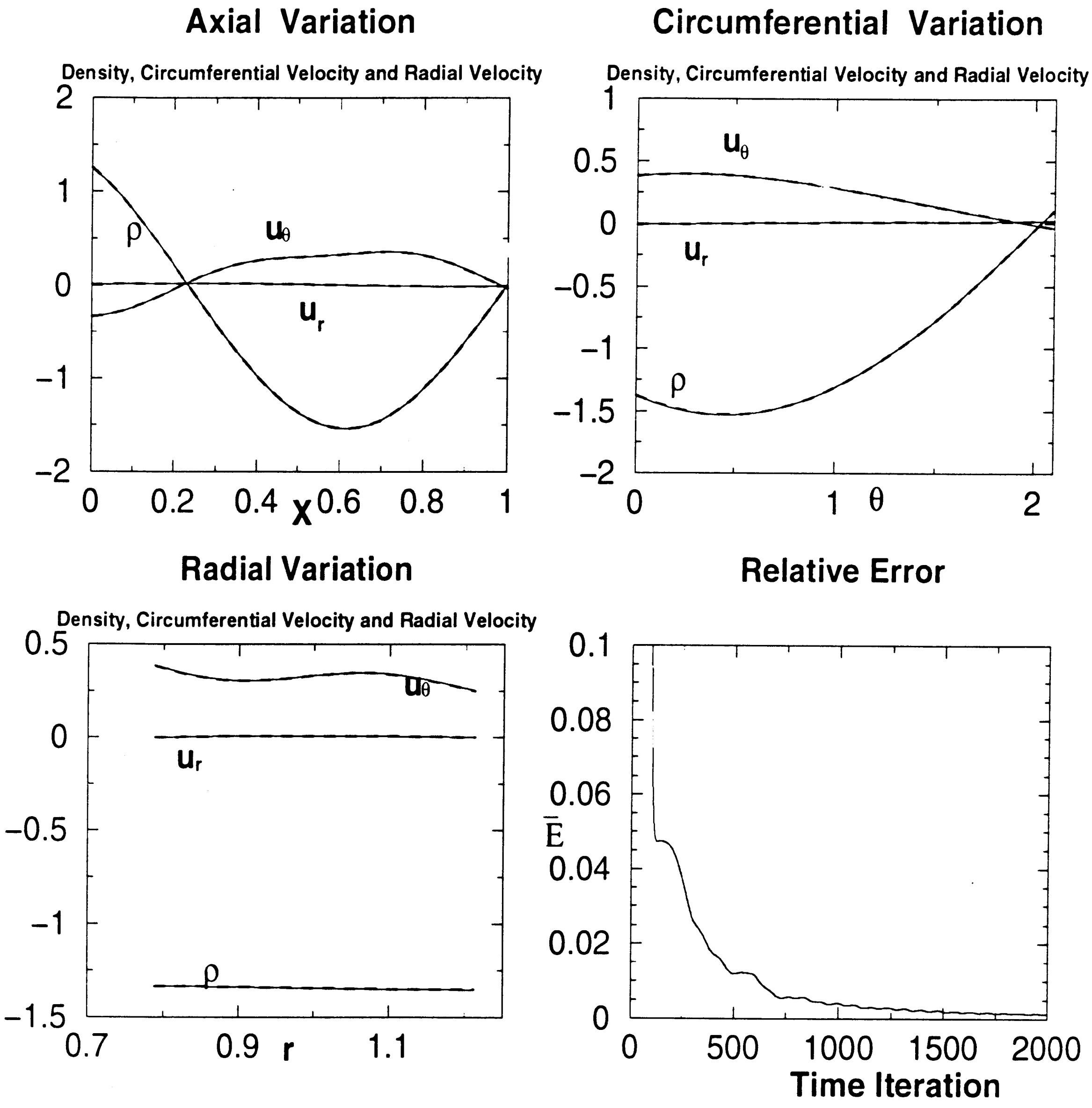
Axial Variation

Circumferential Variation

Radial Variation

Relative Error

Figure 14: A superposition of a vortical and an acoustic disturbance is imposed upstream The hub-tip ratio is .65 and the radial phase variation is such that two full wavelengths fits between the hub and the tip. The numerical solution of the density and two components of the velocity are plotted as solid lines as a function of x, θ and r at the midplanes of the duct respectively. The exact solution is shown by the dashed lines. The global relative error of the density is plotted in the bottom right figure as a function of time iteration.

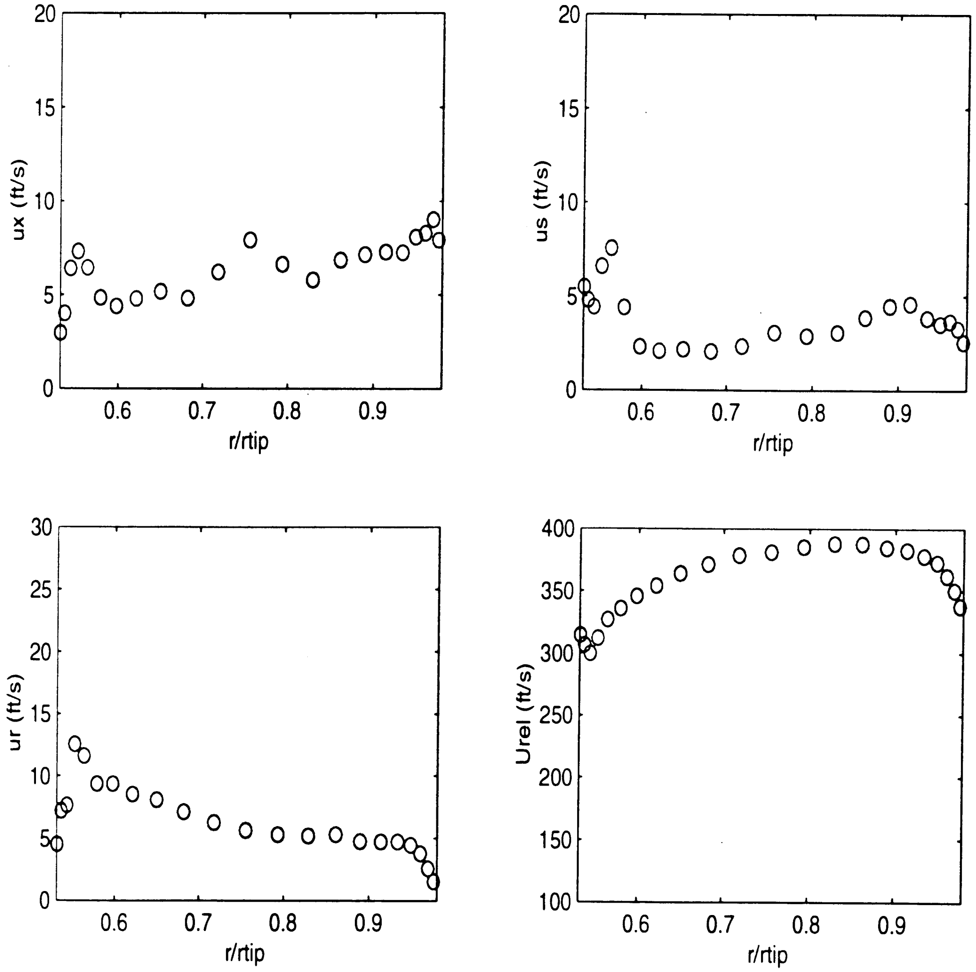

Figure 15: The velocity field of the two times blade passing frequency harmonic resulting from a wake shed from an upstream fan. The computational results were obtained using a Reynolds averaged Navier-Stokes code. Note that the velocity field is fully three-dimensional and that the axial,circumferential and radial velocity components are all the same order of magnitude.

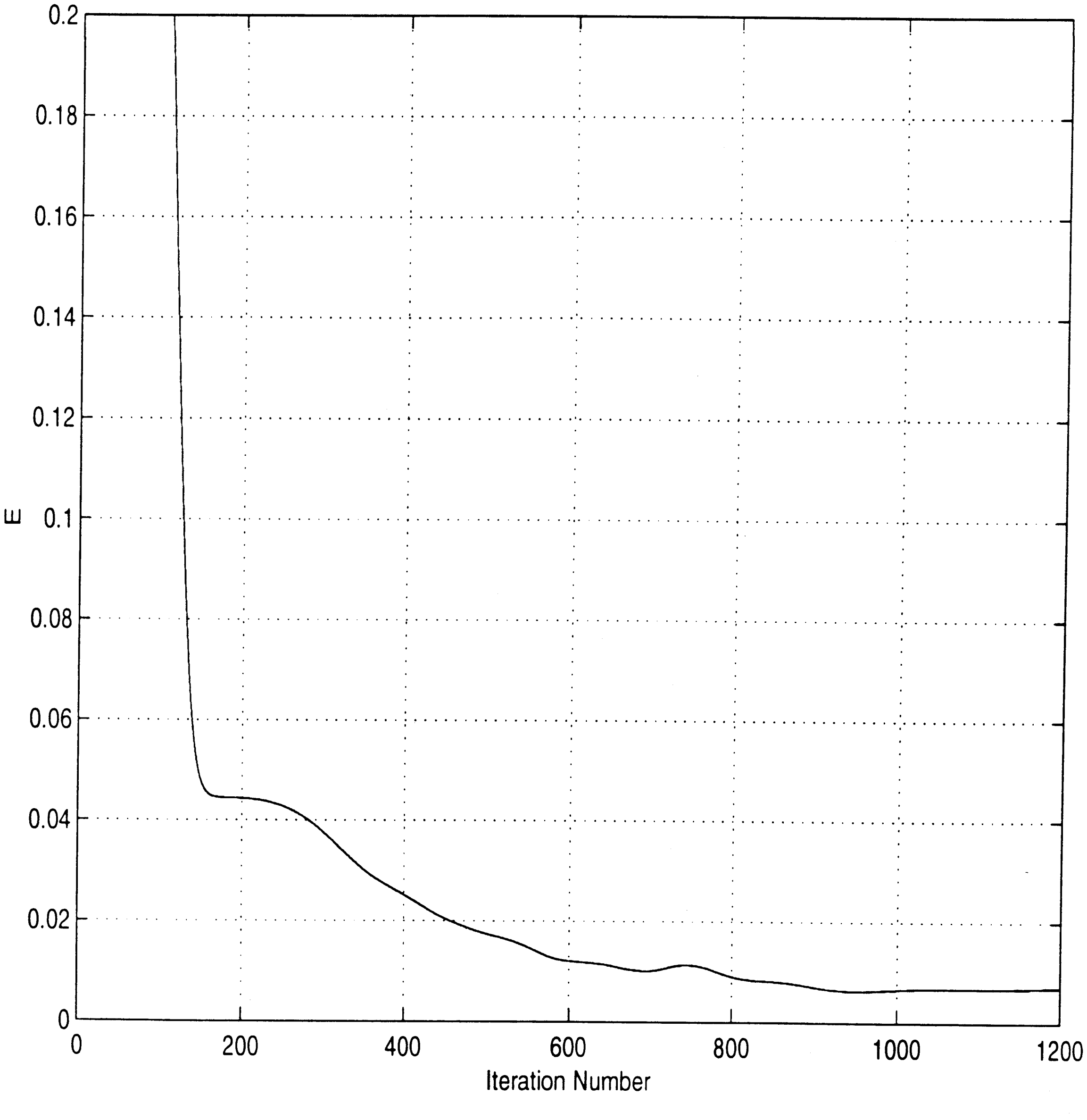

Figure 16: The convergence history for the propagation of an acoustic wave in a free vortex swirling flow. The reduced frequency, spinning mode order, and hub-tip ratio for the case are 24.18, −12, .65, respectively. The convergence parameter, E, is the relative error in the Euler calculation where the 'exact' solution is the eigensolution computed from the normal mode analysis.The free vortex mean flow is chosen such that the swirl Mach number at the mean radius is .4.

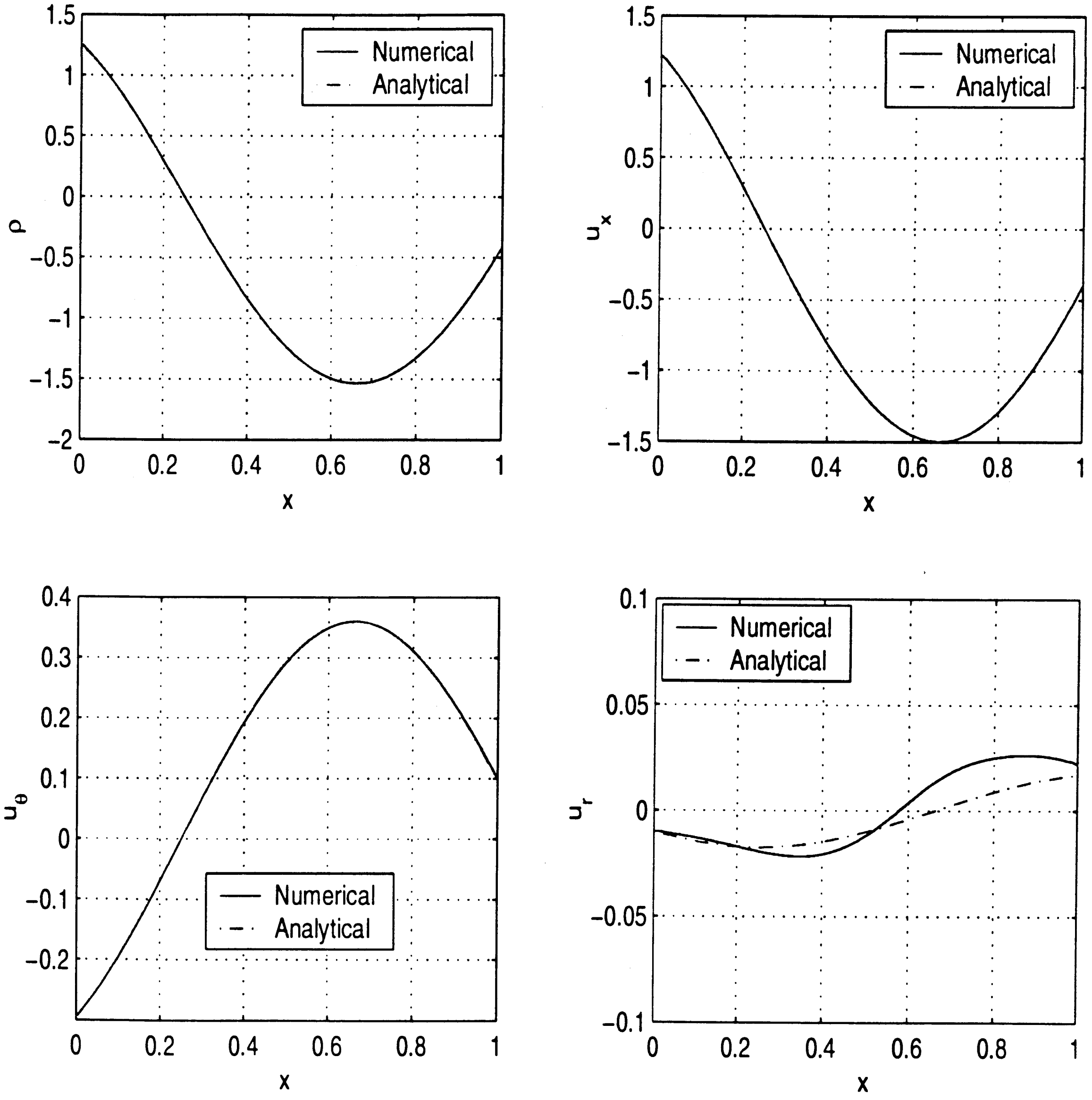

Figure 17: The axial variation of the converged Euler solution is compared with the eigensolution obtained from the normal mode analysis. The numerical solution is denoted by the solid line and the 'exact' solution is denoted by the dashed line. The good agreement between the numerical and analytical solution even at the exit of the domain show the accuracy of the numerical scheme and the nonreflecting boundary conditions. The Euler solution contains eighty points in the axial direction.

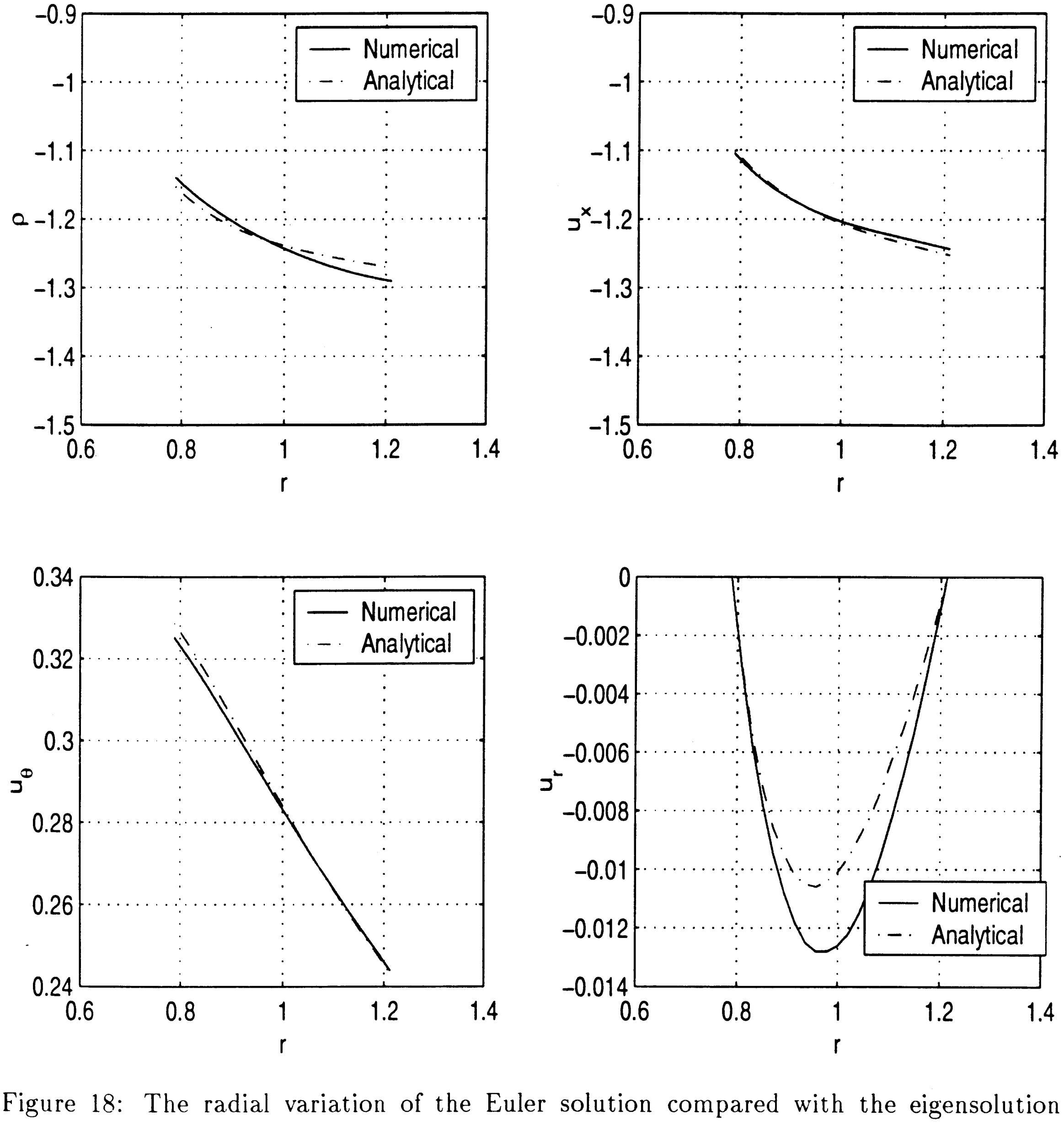

Figure 18: The radial variation of the Euler solution compared with the eigensolution obtained from the normal mode analysis. The numerical solution is denoted by the solid line and the 'exact' solution is denoted by the dashed line. The Euler solution contains twenty points from hub to tip.

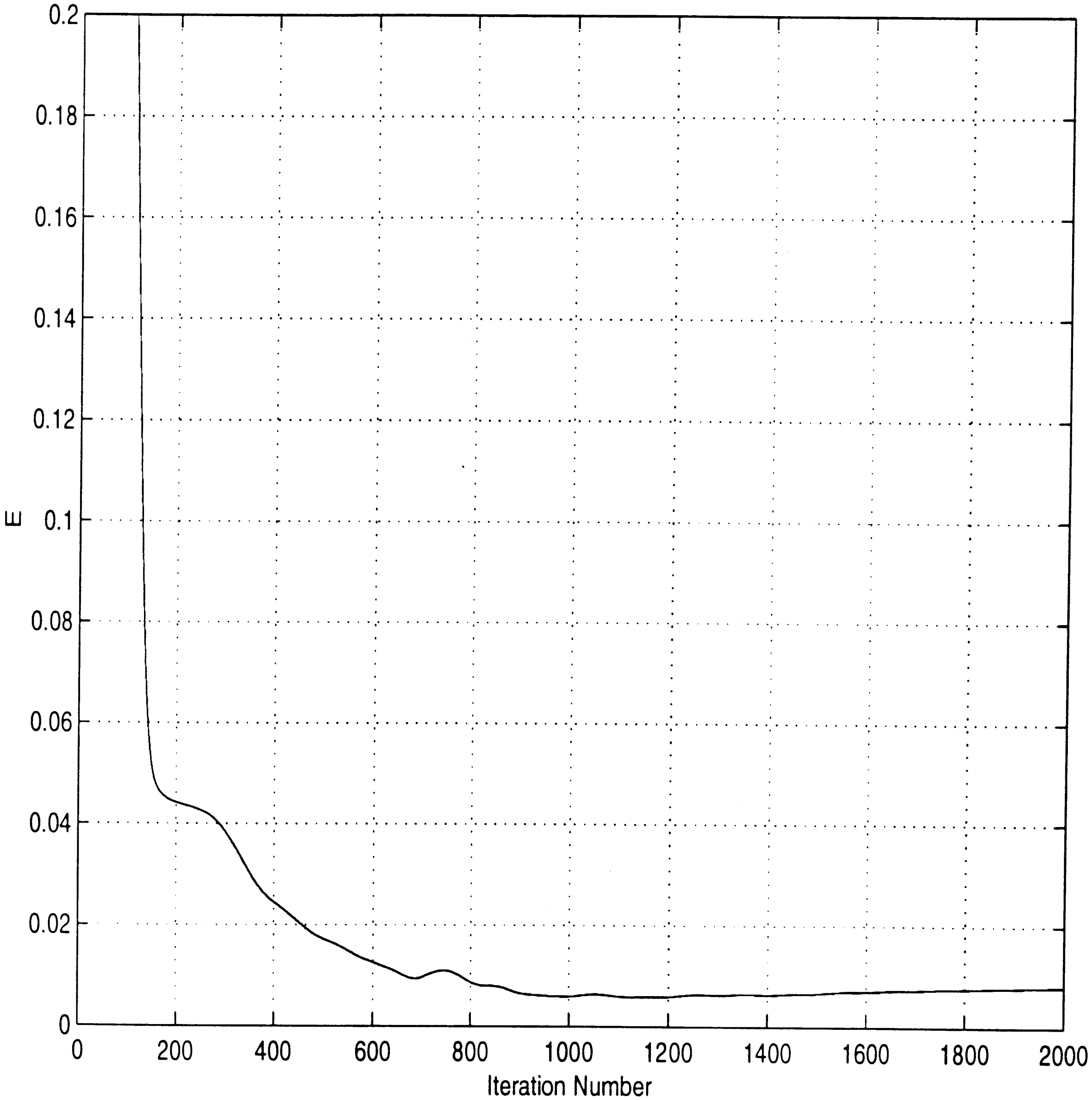

Figure 19: The convergence history for the propagation of an acoustic wave in a rigid body swirling flow. The convergence parameter, E, is the relative error in the Euler calculation where the 'exact' solution is the eigensolution computed from the normal mode analysis

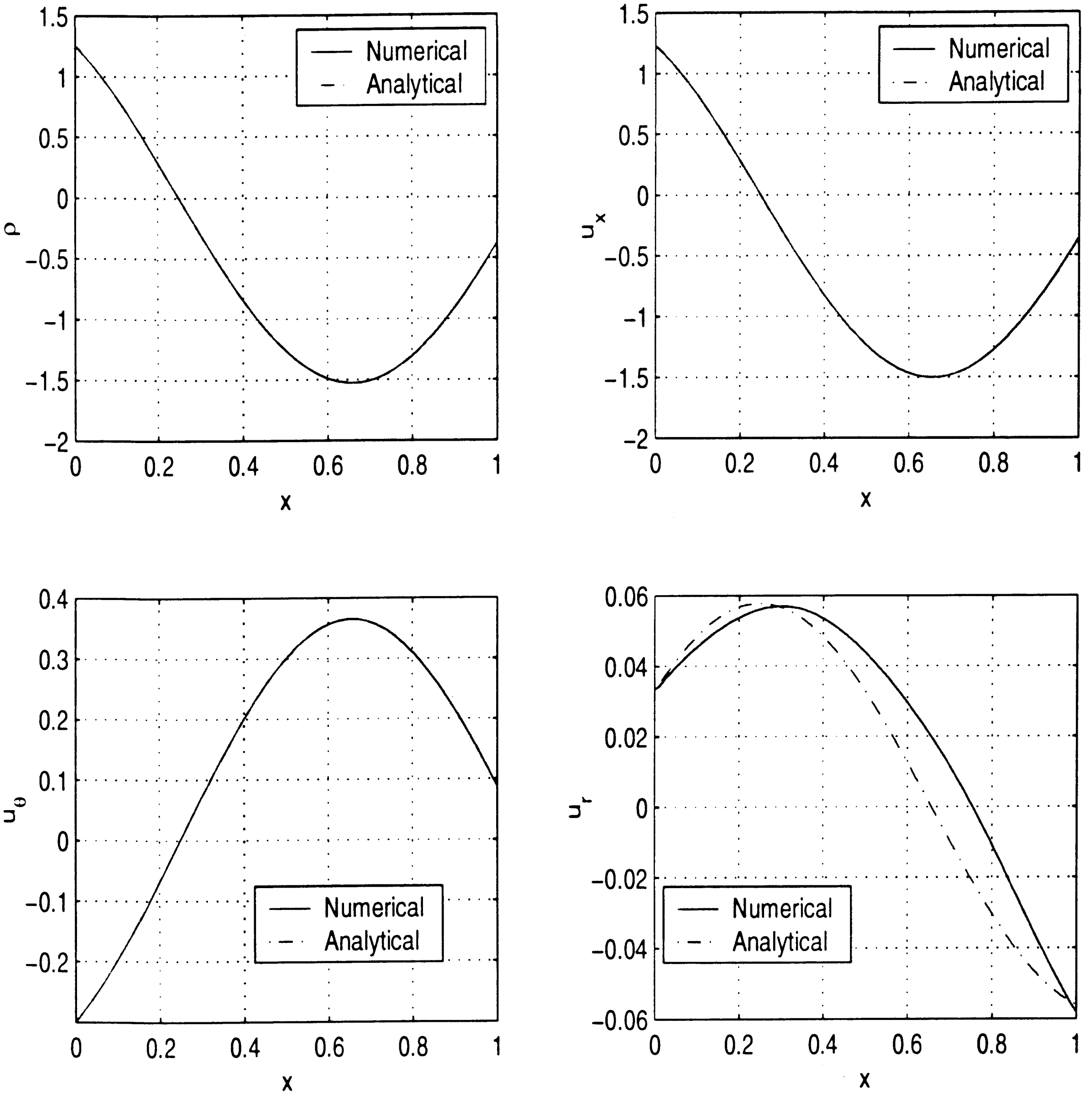

Figure 20: The axial variation of the Euler solution compared with the eigensolution obtained from the normal mode analysis. The Euler solution is denoted by the solid line and the 'exact' eigensolution is denoted by the dashed line. The good agreement between the numerical and analytical solution even at the exit of the domain show the accuracy of the numerical scheme and the nonreflecting boundary conditions. The Euler solution contains eighty points in the axial direction.

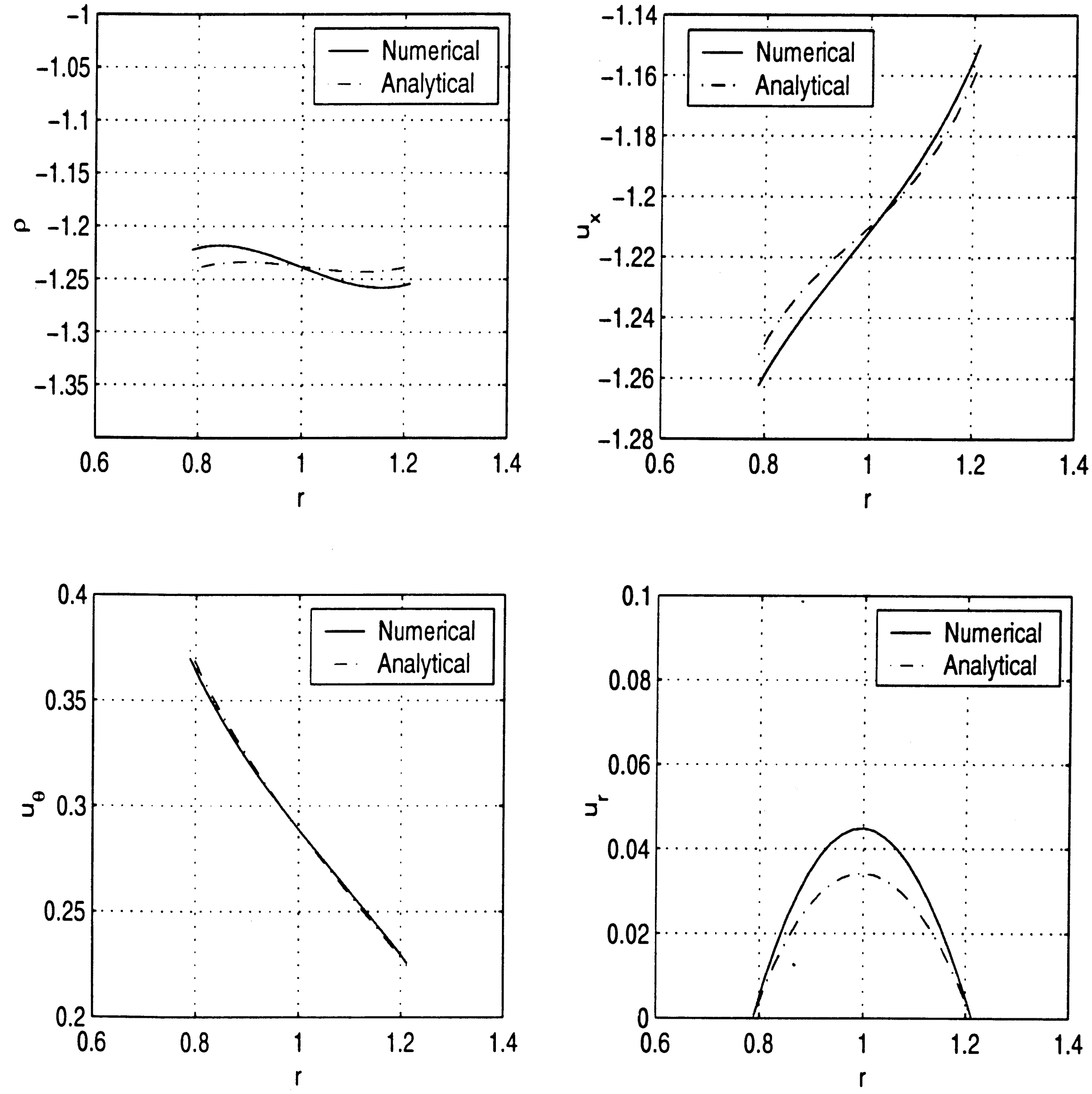

Figure 21: The radial variation of the Euler solution compared with the eigensolution obtained from the normal mode analysis. The numerical solution is denoted by the solid line and the 'exact' eigensolution is denoted by the dashed line. The Euler solution contains twenty points from hub to tip.

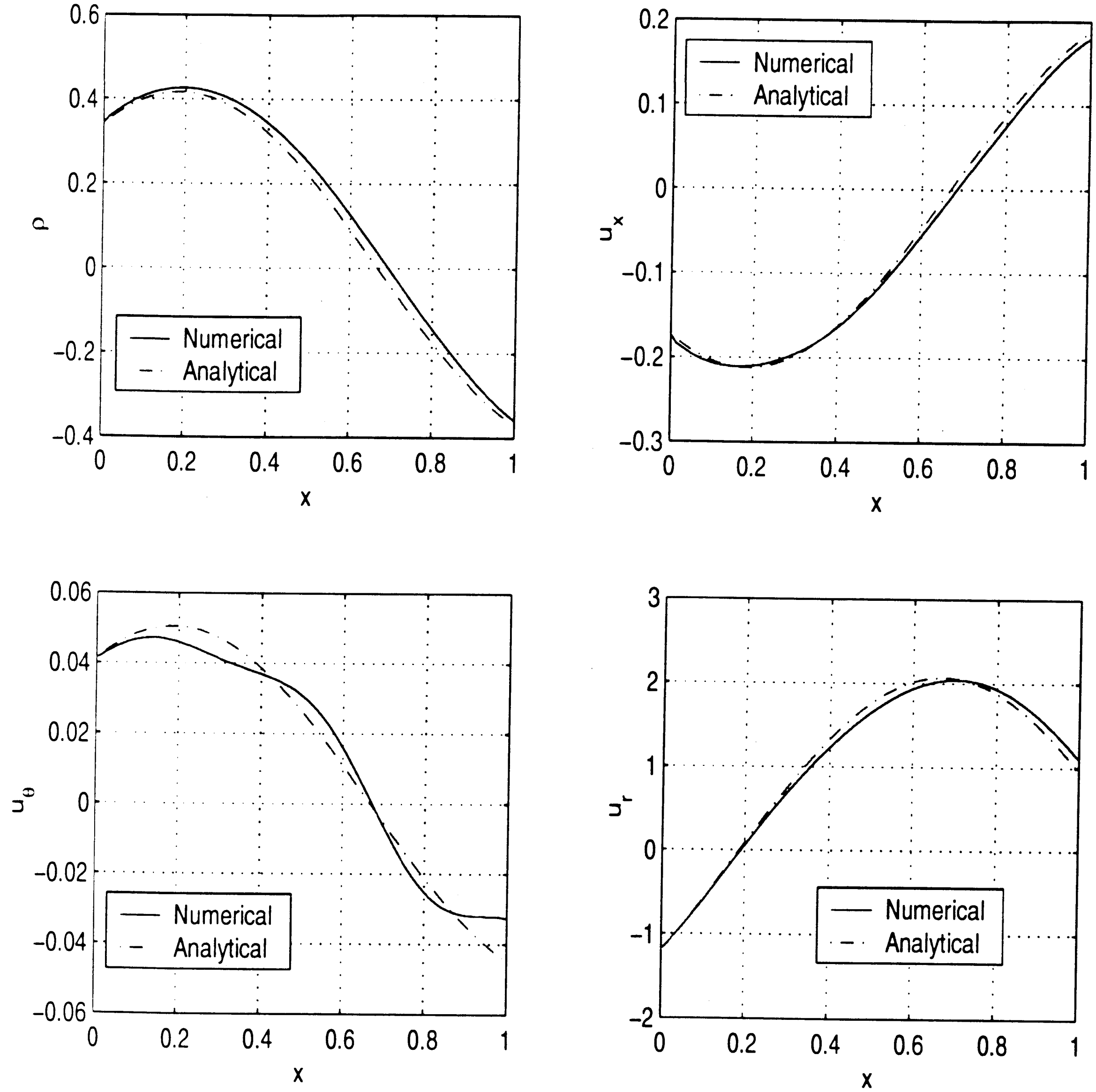

Figure 22: The axial variation of the Euler solution compared with the eigensolution obtained from the normal mode analysis. The Euler solution is denoted by the solid line and the 'exact' eigensolution is denoted by the dashed line. The good agreement between the numerical and analytical solution even at the exit of the domain show the accuracy of the numerical scheme and the nonreflecting boundary conditions. The Euler solution contains eighty points in the axial direction.

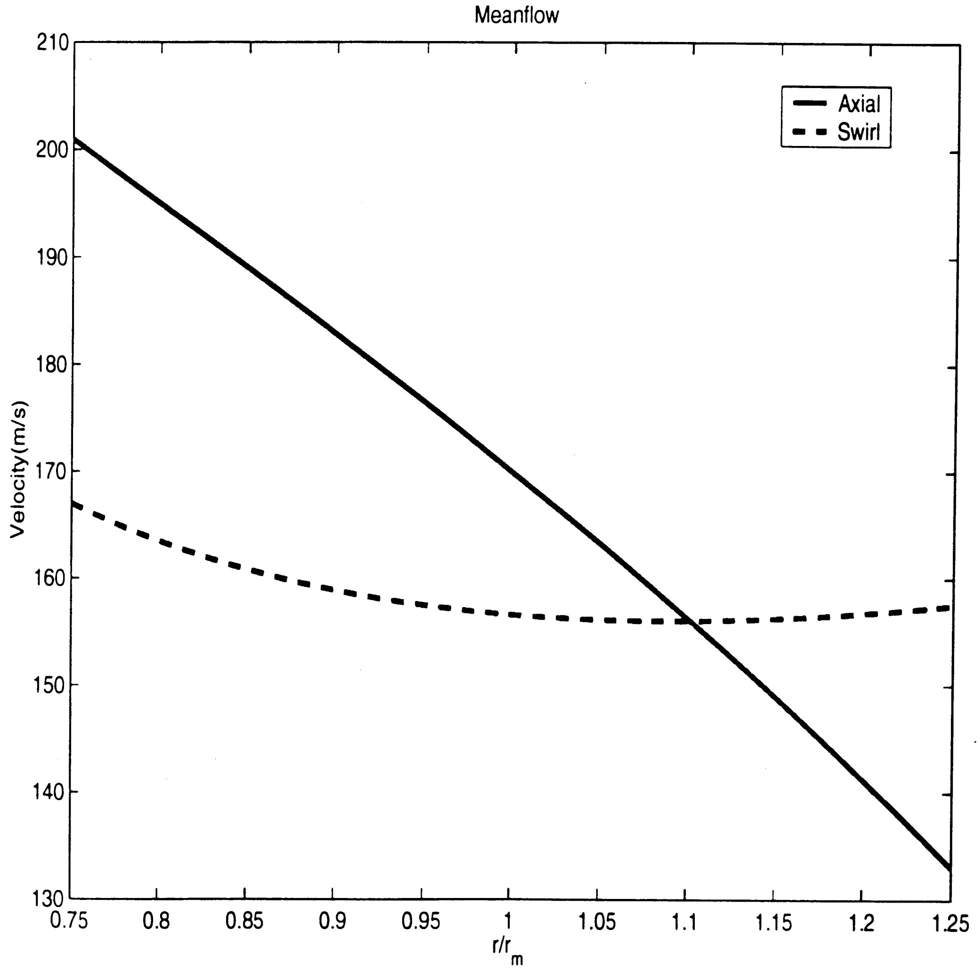

Figure 23: The swirl and axial mean flow distribution representative of the flow between a fan and a fan-exit guide vane for a jet engine.

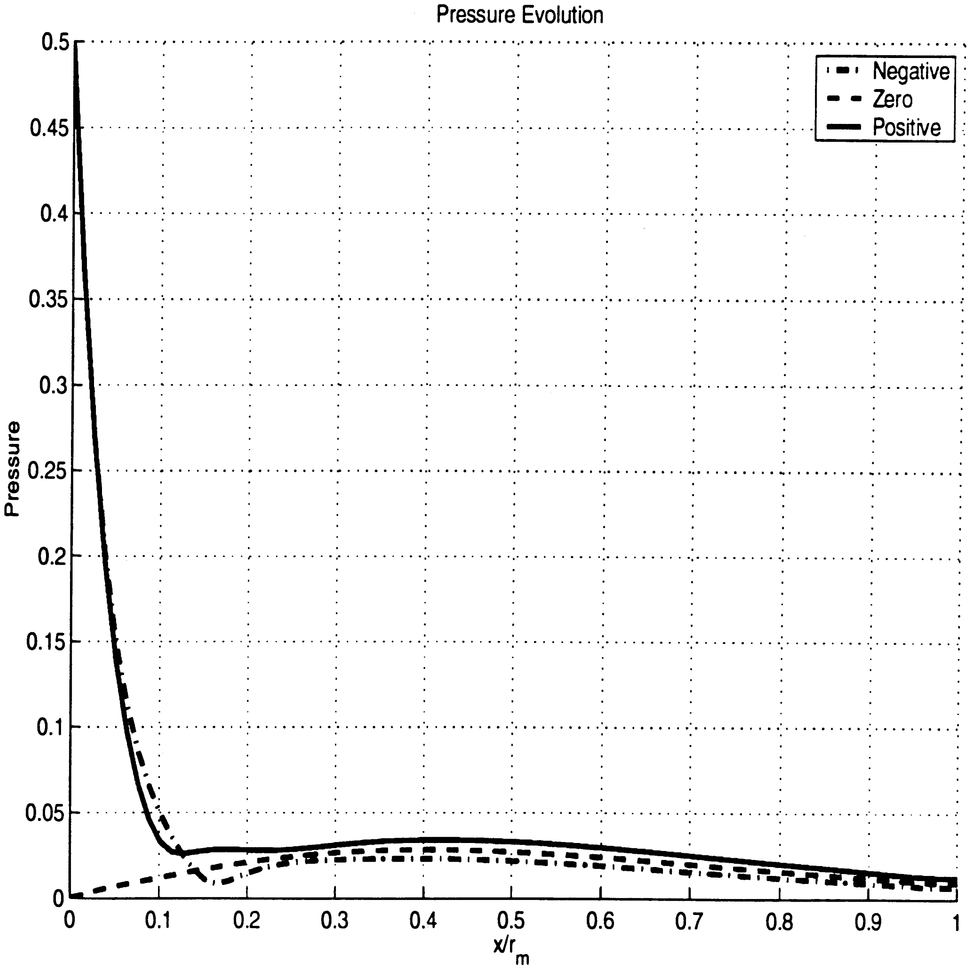

Figure 24: The evolution of the pressure amplitude for three different gust inflow conditions described by $u_x = f_1(r), u_\theta = f_2(r), u_r = 0$ and $p = p_m \sin[\pi i \frac{(r-r_h)}{(r_t-r_h)}]$ where $f_1(r), f_2(r)$ are given and $p_m = +.5, 0, -.5$.

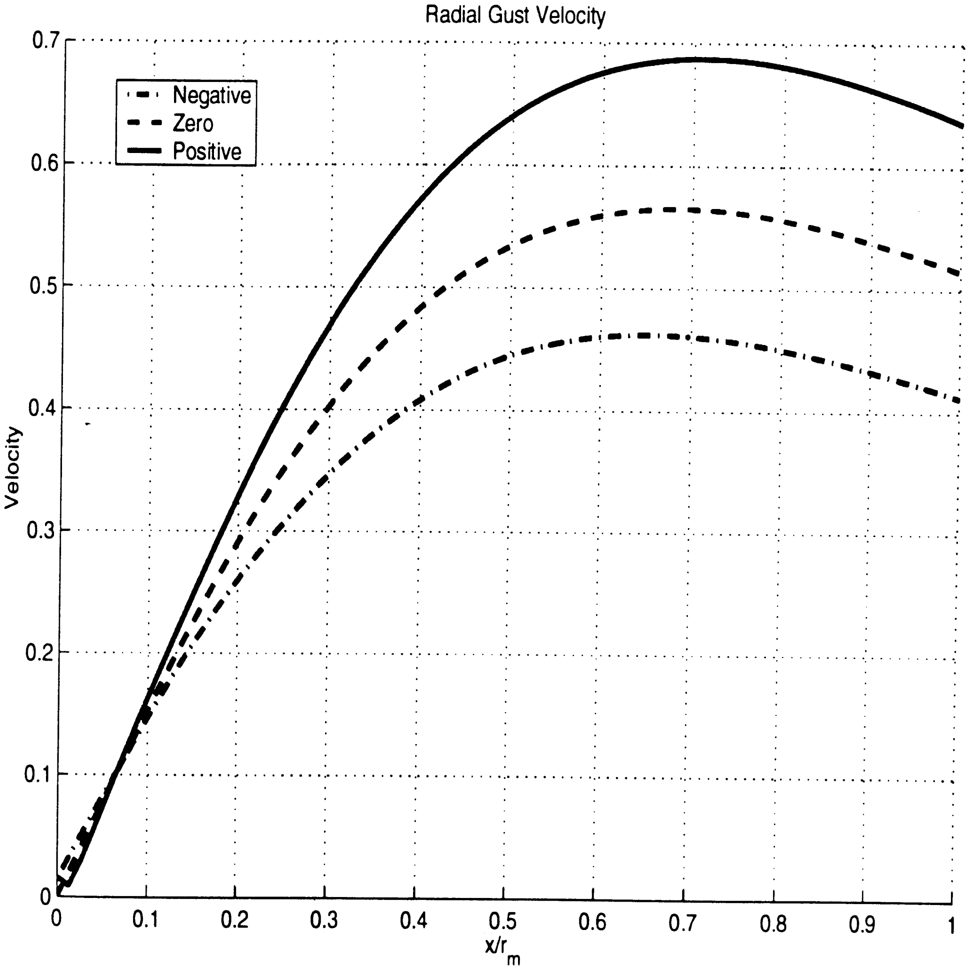

Figure 25: The evolution of the radial velocity amplitude for three different gust inflow conditions described by $u_x = f_1(r), u_\theta = f_2(r), u_r = 0$ and $p = p_m \sin[\pi i \frac{(r-r_h)}{(r_t-r_h)}]$ where $f_1(r), f_2(r)$ are given and $p_m = +.5, 0, -.5$.

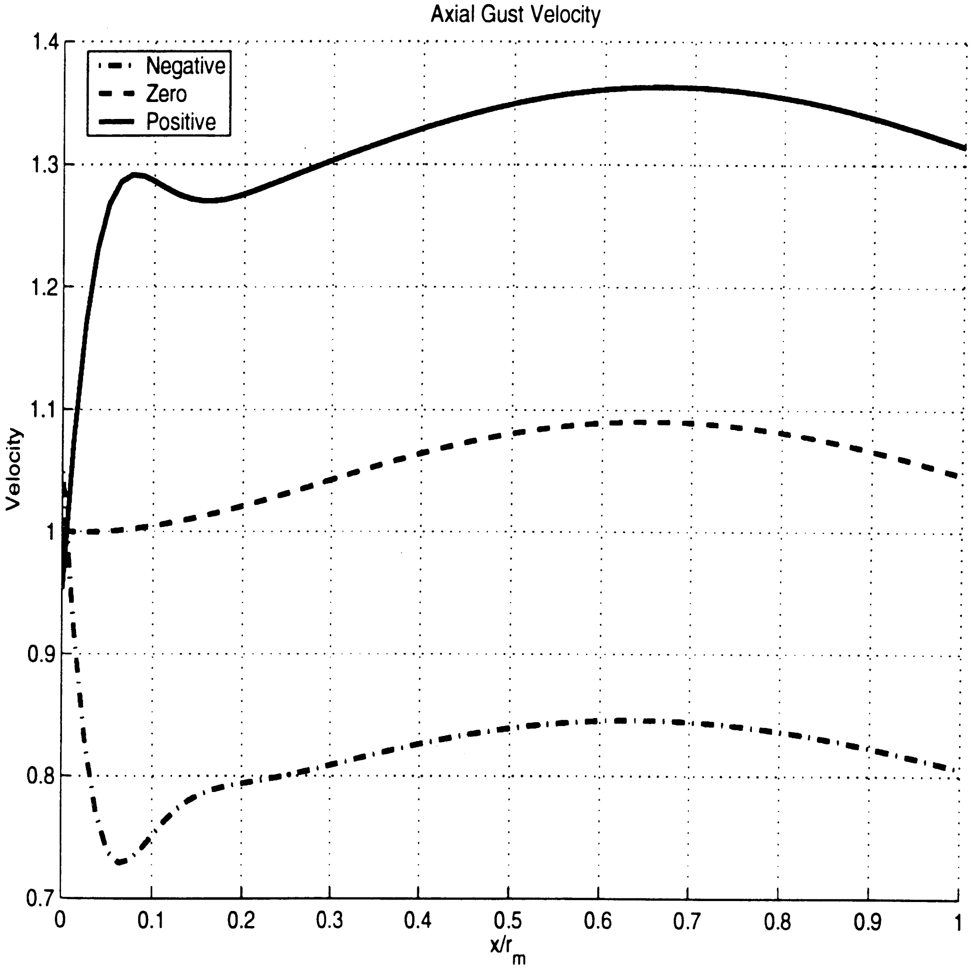

Figure 26: The evolution of the axial velocity amplitude for three different gust inflow conditions described by $u_x = f_1(r), u_\theta = f_2(r), u_r = 0$ and $p = p_m \sin[\pi i \frac{(r-r_h)}{(r_t-r_h)}]$ where $f_1(r), f_2(r)$ are given and $p_m = +.5, 0, -.5$.

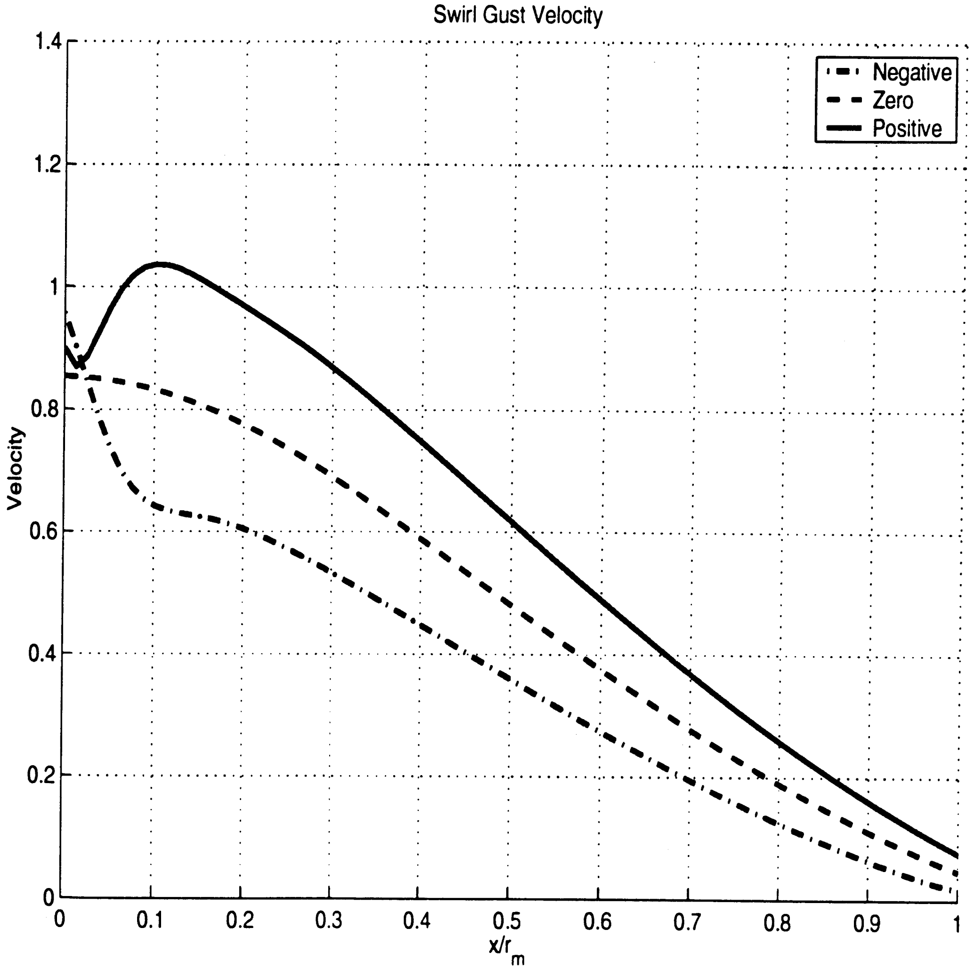

Figure 27: The evolution of the swirl velocity amplitude for three different gust inflow conditions described by $u_x = f_1(r), u_\theta = f_2(r), u_r = 0$ and $p = p_m \sin[\pi i \frac{(r-r_h)}{(r_t-r_h)}]$ where $f_1(r), f_2(r)$ are given and $p_m = +.5, 0, -.5$.

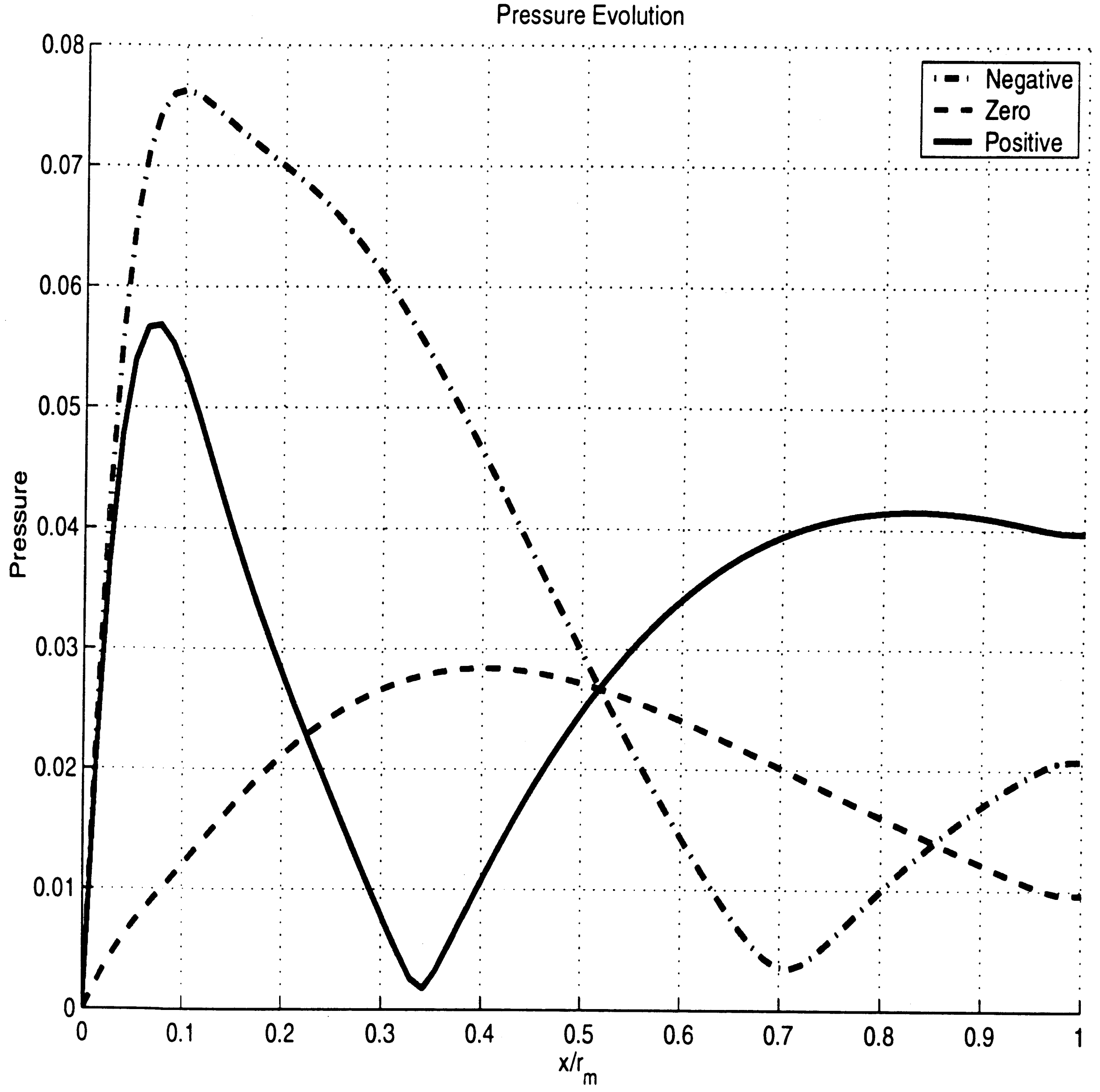

Figure 28: The evolution of the pressure amplitude for three different gust inflow conditions described by $u_x = f_1(r), u_\theta = f_2(r), u_r == u_{mr} \sin[\pi i \frac{(r-r_h)}{(r_t-r_h)}]$ and $p = 0$ where $f_1(r), f_2(r)$ are given and $u_{mr} = +.5, 0, -.5$.

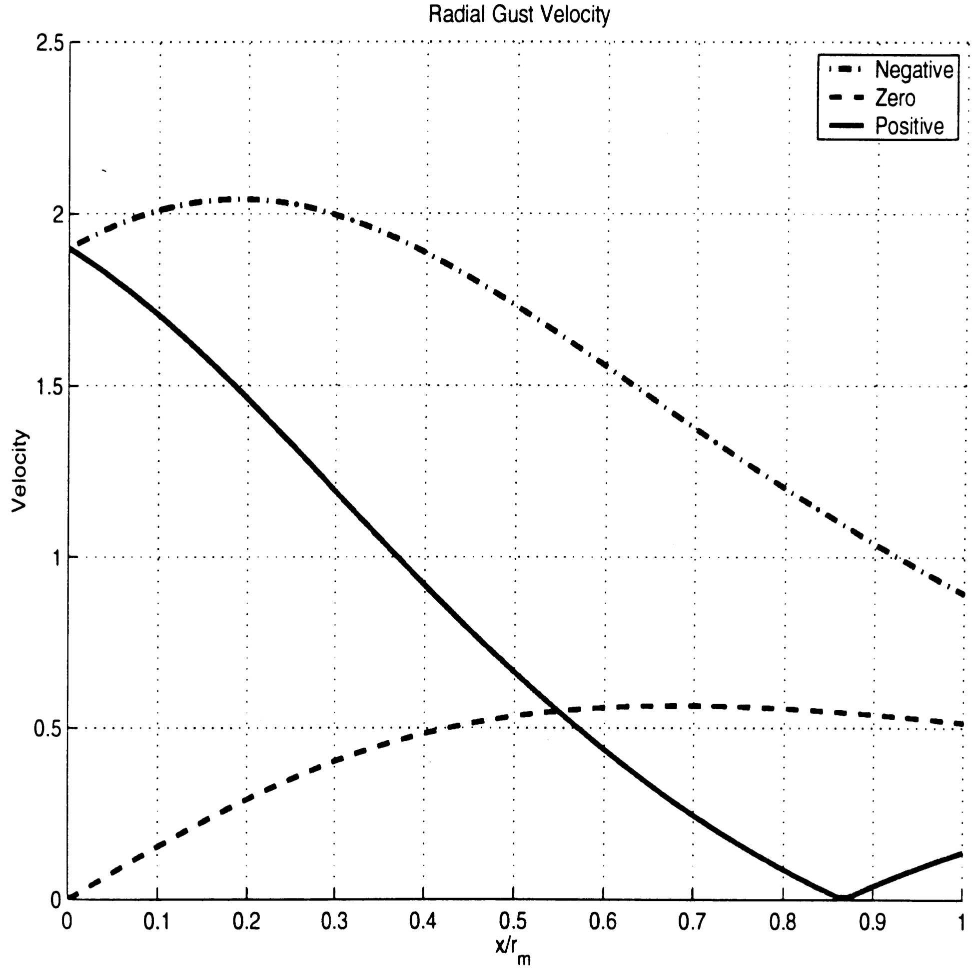

Figure 29: The evolution of the radial velocity amplitude for three different gust inflow conditions described by $u_x = f_1(r), u_\theta = f_2(r), u_r == u_{mr} \sin[\pi i \frac{(r-r_h)}{(r_t-r_h)}]$ and $p = 0$ where $f_1(r), f_2(r)$ are given and $u_{mr} = +.5, 0, -.5$.

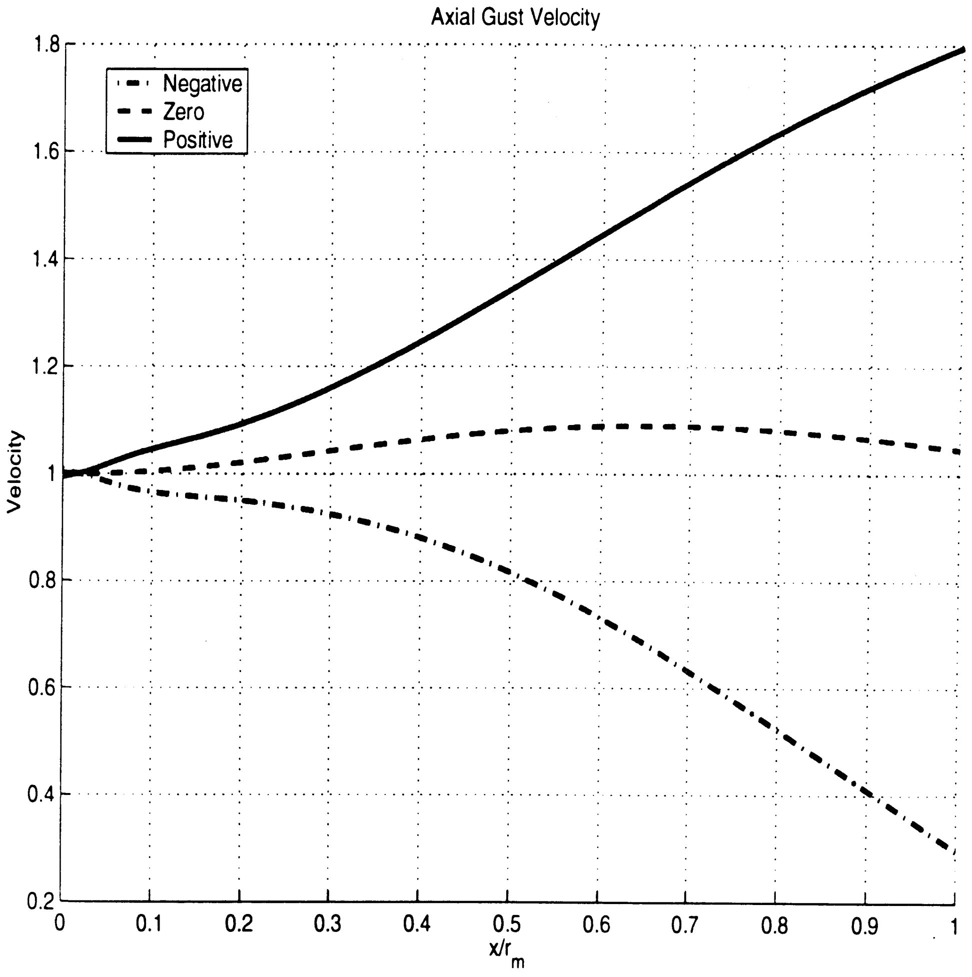

Figure 30: The evolution of the axial velocity amplitude for three different gust inflow conditions described by $u_x = f_1(r), u_\theta = f_2(r), u_r == u_{mr}\sin[\pi i\frac{(r-r_h)}{(r_t-r_h)}]$ and $p = 0$ where $f_1(r). f_2(r)$ are given and $u_{mr} = +.5, 0, -.5$.

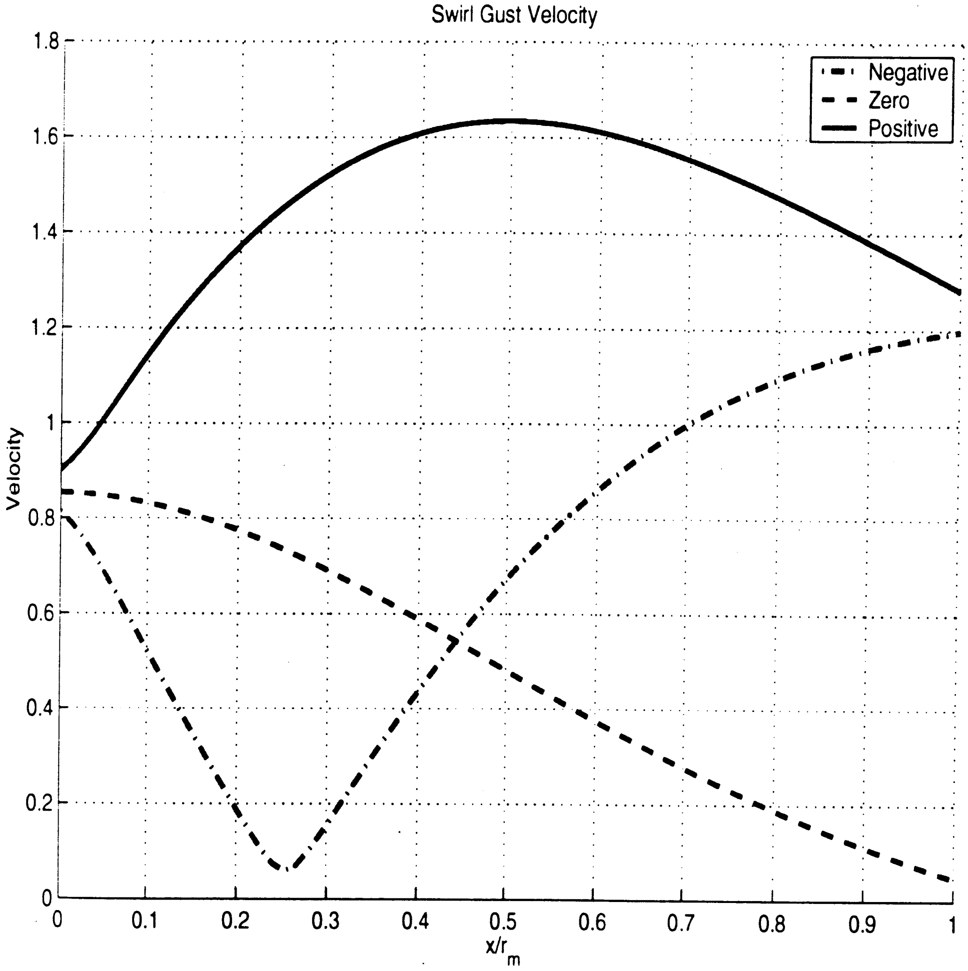

Figure 31: The evolution of the swirl velocity amplitude for three different gust inflow conditions described by $u_x = f_1(r), u_\theta = f_2(r), u_r == u_{mr}\sin[\pi i\frac{(r-r_h)}{(r_t-r_h)}]$ and $p = 0$ where $f_1(r), f_2(r)$ are given and $u_{mr} = +.5, 0, -.5$.

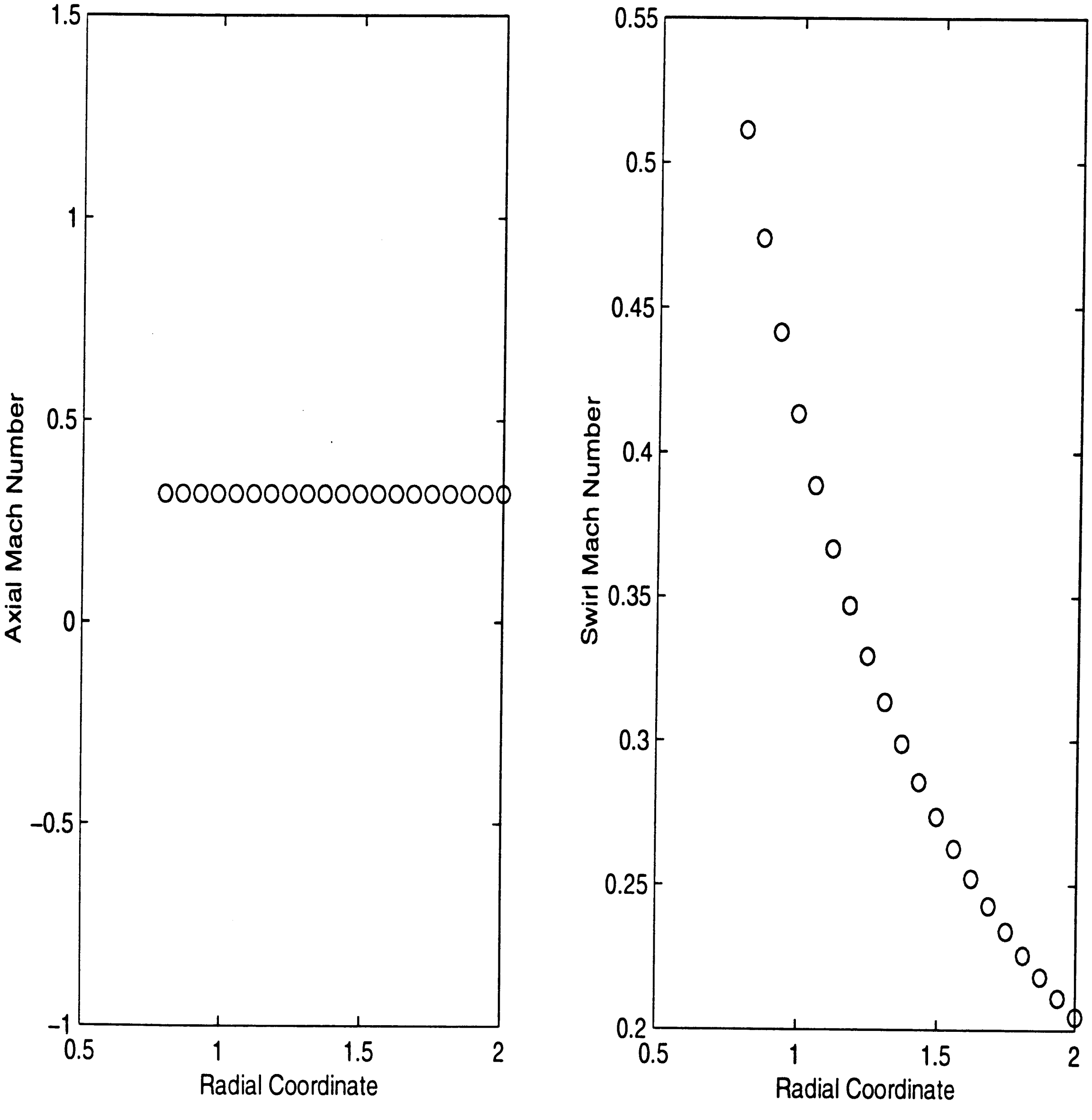

Figure 32: Free vortex swirl distribution for a duct with hub-tip ratio of .4.

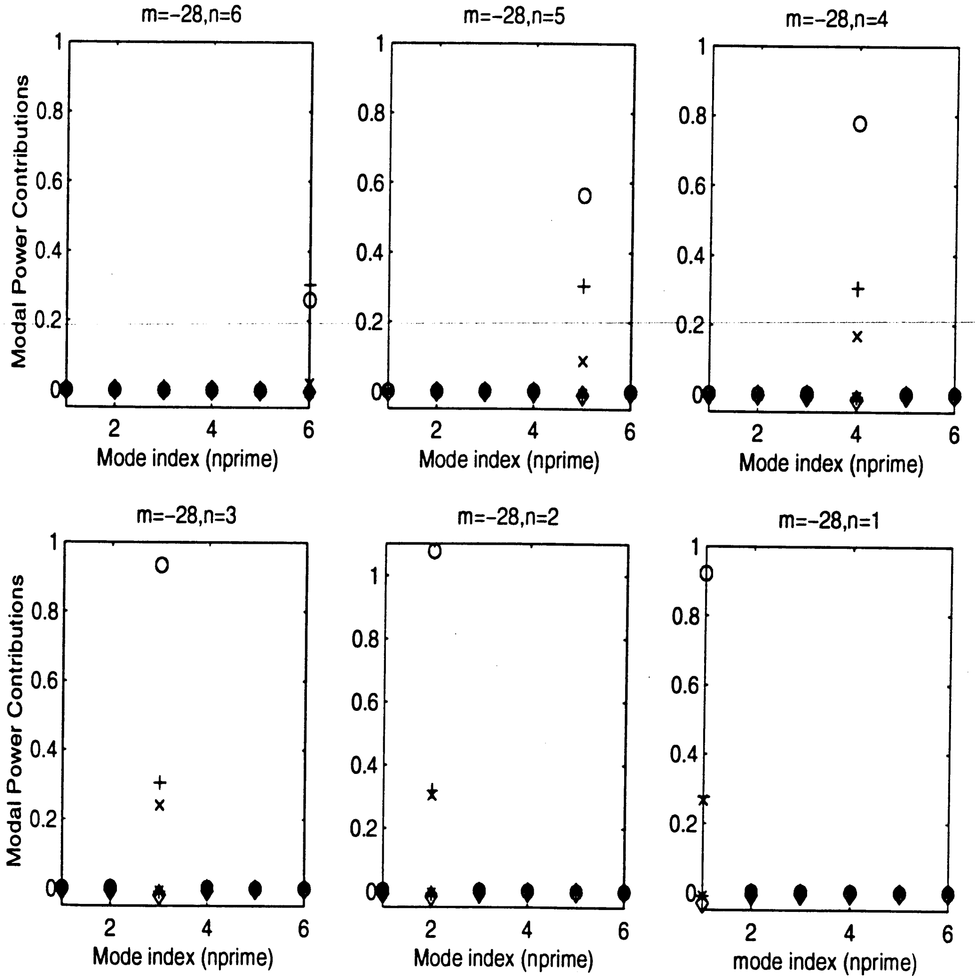

Figure 33: Contributions of each term in (79) to the sound power of the downstream propagating duct modes. The reduced frequency is $\omega = 20$ and $m = -1$. The abscissa is the radial mode index, n' and each figure corresponds to the contribution of each radial mode n. The top row going from left to right correspond to $n = 6, 5, 4$ in descending order and the bottom row going from left to right $n = 3, 2, 1$.

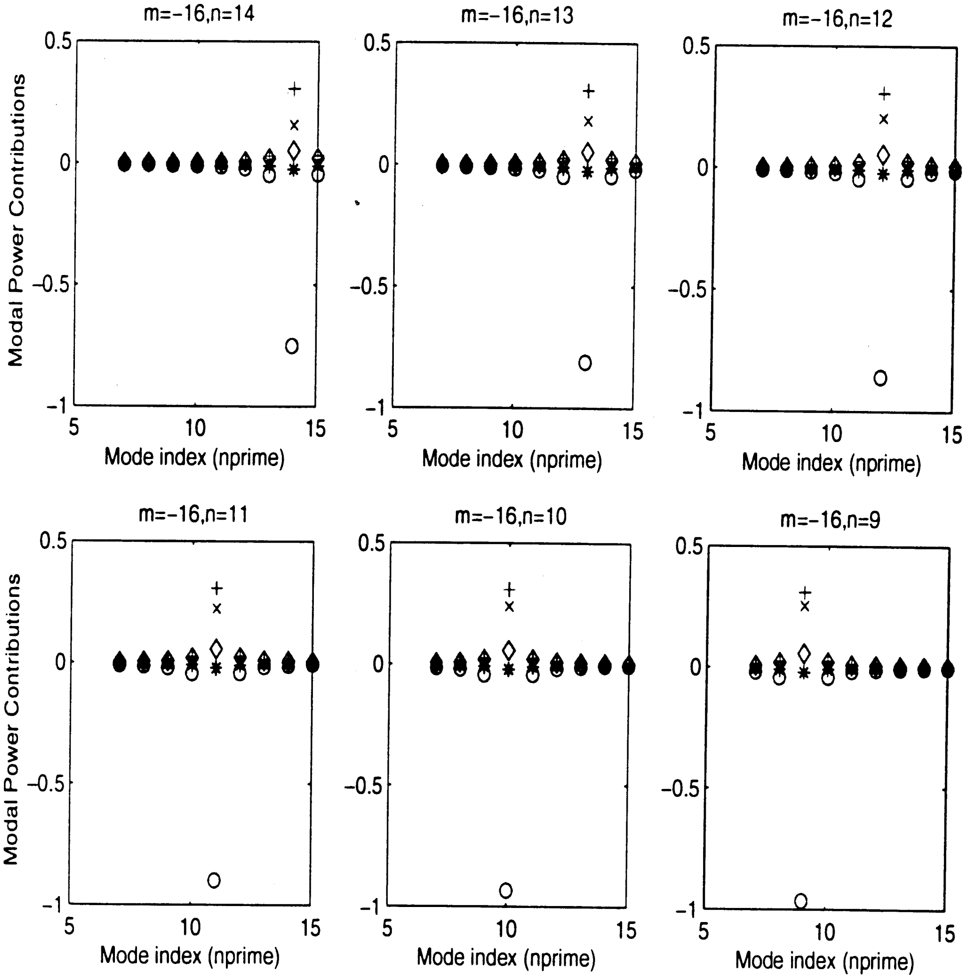

Figure 34: Contributions of each term in (79) to the sound power of the downstream propagating duct modes. The reduced frequency is $\omega = 50$ and $m = -16$. The abscissa is the radial mode index, n' and each figure corresponds to the contribution of each radial mode n. The top row going from left to right correspond to $n = 16, 15, 14$ in descending order and the bottom row going from left to right $n = 13, 12, 11$.

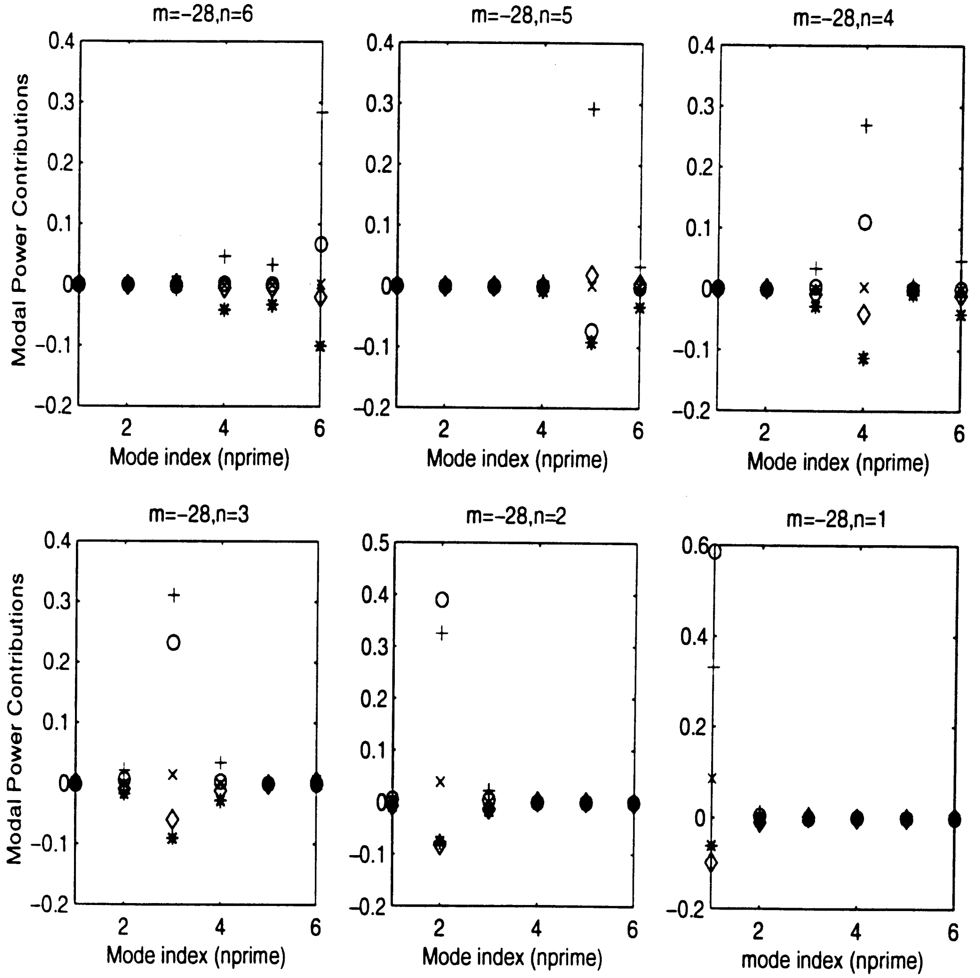

Figure 35: Contributions of each term in (79) to the sound power of the downstream propagating duct modes. The reduced frequency is $\omega = 24.5$ and $m = -28$. The abscissa is the radial mode index, n' and each figure corresponds to the contribution of each radial mode n. The top row going from left to right correspond to $n = 6, 5, 4$ in descending order and the bottom row going from left to right $n = 3, 2, 1$.

REPORT DOCUMENTATION PAGE

Form Approved
OMB No. 0704-0188

1. AGENCY USE ONLY (*Leave blank*)

2. REPORT DATE
December 2003

3. REPORT TYPE AND DATES COVERED
Final Contractor Report

4. TITLE AND SUBTITLE
Inflow/Outflow Conditions for Unsteady Aerodynamics and Aeroacoustics in Nonuniform Flow

5. FUNDING NUMBERS
WBS–22–781–30–11
WU–522–81–16
NAS3–12310

6. AUTHOR(S)
Oliver V. Atassi

7. PERFORMING ORGANIZATION NAME(S) AND ADDRESS(ES)
Pratt & Whitney
400 Main Street
East Hartford, Connecticut, 06108

8. PERFORMING ORGANIZATION REPORT NUMBER
E–13898

9. SPONSORING/MONITORING AGENCY NAME(S) AND ADDRESS(ES)
National Aeronautics and Space Administration
Washington, DC 20546–0001

10. SPONSORING/MONITORING AGENCY REPORT NUMBER
NASA CR—2003-212311

11. SUPPLEMENTARY NOTES

Project Manager, Joseph E. Grady, Aeronautics Directorate, NASA Glenn Research Center, organization code 2600, 216–433–6728.

12a. DISTRIBUTION/AVAILABILITY STATEMENT
Unclassified - Unlimited
Subject Category: 71 Distribution: Nonstandard

Available electronically at http://gltrs.grc.nasa.gov
This publication is available from the NASA Center for AeroSpace Information, 301–621–0390.

12b. DISTRIBUTION CODE

13. ABSTRACT ***(Maximum 200 words)***

The effect of a nonuniform mean flow on the normal modes; the inflow/outflow nonreflecting boundary conditions; and the sound power are studied. The normal modes in an annular duct are computed using a spectral method in combination with a shooting method. The swirl causes force imbalance which couples the acoustic and vortical modes. The acoustic modes are distinguished from the vortical modes by their large pressure and small vorticity content. The mean swirl also produces a Doppler shift in frequency. This results in more counter-spinning modes cut-on at a given frequency than modes spinning with the swirl. Nonreflecting boundary conditions are formulated using the normal mode solutions. The inflow/outflow boundary conditions are implemented in a linearized Euler scheme and validated by computing the propagation of acoustic and vortical waves in a duct for a variety of swirling mean flows. Numerical results show that the evolution of the vortical disturbances is sensitive to the inflow conditions and the details of the wake excitations. All three components of the wake velocity must be considered to correctly compute the wake evolution and the blade upwash. For high frequencies, the acoustic-vortical mode coupling is weak and a conservation equation for the acoustic energy can be derived. Sound power calculations show significant mean flow swirl effects, but mode interference effects are small.

14. SUBJECT TERMS
Aeroacoustics; Unsteady aerodynamics; Euler equations of motion; Engine noise

15. NUMBER OF PAGES
84

16. PRICE CODE

17. SECURITY CLASSIFICATION OF REPORT	**18. SECURITY CLASSIFICATION OF THIS PAGE**	**19. SECURITY CLASSIFICATION OF ABSTRACT**	**20. LIMITATION OF ABSTRACT**
Unclassified	Unclassified	Unclassified	